

ON THE IMPORTANCE OF THE EQUATION OF STATE FOR THE NEUTRINO-DRIVEN SUPERNOVA EXPLOSION MECHANISM

YUDAI SUWA¹, TOMOYA TAKIWAKI², KEI KOTAKE^{2,3}, TOBIAS FISCHER^{4,5}, MATTHIAS LIEBENDÖRFER⁶, AND KATSUHIKO SATO⁷

Draft version August 20, 2018

ABSTRACT

By implementing widely-used equations of state (EOS) from Lattimer & Swesty (LS) and H. Shen et al. (SHEN) in core-collapse supernova simulations, we explore possible impacts of these EOS on the post-bounce dynamics prior to the onset of neutrino-driven explosions. Our spherically symmetric (1D) and axially symmetric (2D) models are based on neutrino radiation hydrodynamics including spectral transport, which is solved by the isotropic diffusion source approximation. We confirm that in 1D simulations neutrino-driven explosions cannot be obtained for any of the employed EOS. Impacts of the EOS on the post-bounce hydrodynamics are more clearly visible in 2D simulations. In 2D models of a $15 M_{\odot}$ progenitor using the LS EOS, the stalled bounce shock expands to increasingly larger radii, which is not the case using the SHEN EOS. Keeping in mind that the omission of the energy drain by heavy-lepton neutrinos in the present scheme could facilitate explosions, we find that 2D models of an $11.2 M_{\odot}$ progenitor produce neutrino-driven explosions for all the EOS under investigation. Models using the LS EOS are slightly more energetic compared to those with the SHEN EOS. The more efficient neutrino heating in the LS models coincides with a higher electron antineutrino luminosity and a larger mass that is enclosed within the gain region. The models based on the LS EOS also show a more vigorous and aspherical downflow of accreting matter to the surface of the protoneutron star (PNS). The accretion pattern is essential for the production and strength of outgoing pressure waves, that can push in turn the shock to larger radii and provide more favorable conditions for the explosion. Based on our models we investigate several diagnostic indicators of the explosion that have been suggested in the literature, e.g., the amplitude of the standing-accretion shock instability mode, the mass weighted average entropy in the gain region, the PNS radius, the antesonics condition, the ratio of advection and heating timescales, the neutrino heating efficiency, and the growth parameter of convection.

Subject headings: equation of state — hydrodynamics — neutrinos — stars: neutron — supernovae: general

1. INTRODUCTION

Core-collapse supernova explosions are triggered by the gravitational energy released during the transition from a stellar core to a protoneutron star (PNS). The thermodynamic conditions obtained at the center of the stellar core are temperatures on the order of tens of MeV and densities on the order of normal nuclear matter density ($3 \times 10^{14} \text{ g cm}^{-3}$). There are only few equations of state (EOS) available for these conditions. Several studies by Takahara & Sato (1982) and Baron et al. (1985) were pioneering, investigating the impact of the EOS on the explosion dynamics, albeit in a phenomenological approach (see collective references in Bethe 1990). The most commonly used nuclear EOS in recent supernova simula-

tions are the EOS from Lattimer & Swesty (1991) (hereafter LS), based on the incompressible liquid-drop model including surface effects, and from Shen et al. (1998) (SHEN). The latter is based on relativistic mean field (RMF) theory and the Thomas-Fermi approximation. Recently, a new nuclear RMF EOS has been published in Hempel & Schaffner-Bielich (2010), which in addition can be obtained for several nuclear parametrizations and provides detailed information about the chemical composition (see also Shen et al. 2011; Furusawa et al. 2011).

Thus, extensive studies have been performed to investigate the impact of the nuclear EOS on supernova simulations. But most of these simulations are limited to spherical symmetry. Thompson et al. (2003) investigated the effects of the incompressibility parameter on the evolution of temperature and neutrino luminosities during the postbounce evolution based on the three different incompressibilities of the LS EOS ($K = 180, 220, 375 \text{ MeV}$). Only a small impact on the dynamics was found. Sumiyoshi et al. (2006, 2007) performed long-term simulations of a $40 M_{\odot}$ progenitor star from Woosley & Weaver (1995) comparing LS ($K = 180 \text{ MeV}$) and SHEN, focusing on the evolution until black-hole formation and the emitted neutrino signal. Fischer et al. (2009) included in addition progenitor stars from different stellar evolution groups in the mass range of $40\text{--}50 M_{\odot}$ and studied the neutrino signal and

¹ Yukawa Institute for Theoretical Physics, Kyoto University, Oiwake-cho, Kitashirakawa, Sakyo-ku, Kyoto, 606-8502, Japan

² Center for Computational Astrophysics, National Astronomical Observatory of Japan, Mitaka, Tokyo 181-8588, Japan

³ Division of Theoretical Astronomy, National Astronomical Observatory of Japan, Mitaka, Tokyo 181-8588, Japan

⁴ GSI, Helmholtzzentrum für Schwerionenforschung GmbH, Planckstr. 1, 64291 Darmstadt, Germany

⁵ Institut für Kernphysik, Technische Universität Darmstadt, Schlossgartenstraße 9, 64289 Darmstadt, Germany

⁶ Department of Physics, University of Basel, Klingelbergstr. 82, CH-4056 Basel, Switzerland

⁷ The Institute for the Physics and Mathematics of the Universe, the University of Tokyo, Kashiwa, Chiba, 277-8568, Japan

collapse to a black hole in a systematic way. Their results were confirmed and extended by O'Connor & Ott (2011) applying a simplified treatment of neutrino transport. In Hempel et al. (2012), the authors applied their new EOS and systematically explored the hydrodynamic evolution and emission of neutrinos for different nuclear parameters within the class of RMF EOS. Moreover, Sagert et al. (2009) and Fischer et al. (2011) explored the appearance of quark matter via a first order phase transition in supernova simulations during the early post-bounce phase, which triggers the explosion even in spherically symmetric models.

Furthermore, EOS studies based on multi-dimensional supernova models have become available recently. Kotake et al. (2004) and Scheidegger et al. (2010) performed two-dimensional (2D) and three-dimensional (3D) simulations, respectively, and investigated the initial post-bounce phase and gravitational wave emission focusing on effects of rotation and convection with simplified neutrino treatments. They found that the gravitational wave signal depends strongly on the EOS (e.g., Kotake 2011 for a recent review). In addition, Marek et al. (2009) investigated the EOS dependence of high frequency variations of the neutrino luminosity and gravitational wave emission by performing 2D simulations that include detailed neutrino-radiative transfer.

Several 2D studies obtain neutrino-driven explosions of massive iron-core progenitors (see e.g. Marek et al. 2009; Bruenn et al. 2009; Suwa et al. 2010; Müller et al. 2012a), aided by the standing accretion-shock instability (SASI) and neutrino-driven convection. These simulations were evolved until the expanding explosion shock left the central core (~ 1000 km) between about 400–600 ms after bounce (depending on the progenitor and details of input physics). Most multi-dimensional supernova studies used the LS EOS with the incompressibility of $K = 180$ MeV, which is a very soft EOS (Buras et al. 2006a; Suwa et al. 2010). In addition, Marek & Janka (2009) performed 2D simulation using the stiffer EOS from Hillebrandt et al. (1984), and found that the softer EOS results in a more optimistic situation for a possible onset of an explosion. However, their simulation with the stiffer EOS had been performed for a shorter post-bounce time than the softer EOS. Hence, a final conclusion cannot be drawn.⁸ Even further, they employed only two EOS, each of which has a different incompressibility and symmetry energy. Note that the entire set of nuclear parameters, not only the incompressibility and the symmetry energy, but also their density dependence determine the resulting EOS.

In this paper we present results of numerical simulations of core-collapse supernovae of massive iron-core progenitors. The spectral neutrino transport is treated by the *Isotropic Diffusion Source Approximation* (IDSA) (Liebendörfer et al. 2009). We employ four EOS of LS (with the three incompressibilities) and SHEN. We apply these different EOS in axially symmetric (2D) simulations and investigate the differences obtained. In the analysis of the data we focus on the post-bounce phase

after the shock-stall, on the neutrino-driven shock revival and the shock propagation for more than 500 ms after core bounce.

The paper opens with the description of the numerical method and the employed EOS in Section 2. The results of 1D and 2D simulations are presented in Section 3 and 4. We summarize our results and discuss their implications in Section 5.

2. SUPERNOVA MODEL

2.1. Hydrodynamics

The basic evolution equations are written as follows,

$$\frac{d\rho}{dt} + \rho \nabla \cdot \mathbf{v} = 0, \quad (1)$$

$$\rho \frac{d\mathbf{v}}{dt} = -\nabla P - \rho \nabla \Phi \quad (2)$$

$$\frac{\partial e^*}{\partial t} + \nabla \cdot [(e^* + P) \mathbf{v}] = -\rho \mathbf{v} \cdot \nabla \Phi + Q_\nu, \quad (3)$$

$$\Delta \Phi = 4\pi G \rho, \quad (4)$$

with rest-mass density ρ , total pressure P (including neutrino contributions), matter velocity \mathbf{v} , total energy density e^* , gravitational potential Φ as well as neutrino heating/cooling rates Q_ν . $\frac{d}{dt}$ is the Lagrangian time derivative and $\frac{\partial}{\partial t}$ is the Eulerian time derivative.

Our 2D simulations are performed using a code which is based on the spectral neutrino transport scheme IDSA, developed by Liebendörfer et al. (2009), and the ZEUS-2D code (Stone & Norman 1992; Suwa et al. 2010, 2011).⁹ Details about the IDSA are given in the next subsection.

In this work we use the conservation form for the total energy rather than the internal energy equation used in the original ZEUS-2D code to improve the accuracy of the total energy conservation. The source term of the self-gravity in Eq. (3) is computed by the method described in Müller et al. (2010). The violation of the energy conservation remains within 0.03% of its gravitational binding energy ($\sim 10^{53}$ erg; see Appendix of Suwa et al. 2011). The simulations are performed on a grid of 300 logarithmically spaced radial zones up to 5000 km and 128 equidistant angular zones covering $0 < \theta < \pi$. For neutrino transport, we use 20 logarithmically spaced energy bins reaching from 3 to 300 MeV.

Our code is written in spherical coordinates, which have the following advantage: We can compare 1D and 2D results of the “same” code. As for 1D simulations, we just use “one” grid for the lateral direction. This is impossible for a Cartesian grid code or a distorted grid code such as VULCAN/2D (Burrows et al. 2006). In fact, results obtained in 1D and 2D simulations show exactly the same features for the preshocked region (see Figure 1 of Suwa et al. 2010). Furthermore, using the detailed comparison study of, e.g., Liebendörfer et al. (2005) based on spherically symmetric simulations, it is possible to validate our code (see Appendix in Suwa et al. 2011).

⁸ Employing a stiffer EOS with $K = 263$ MeV based on the Hartree-Fock approximation, Marek et al. found no explosions for the same progenitor model, whereas they indeed obtained an explosion for Shen EOS that is even stiffer with $K = 281$ MeV (see, e.g., Janka 2012).

⁹ Our code was developed for core-collapse simulation and was used for the core collapse of very massive Population III stars (Suwa et al. 2007a,b, 2009), where a leakage scheme for neutrinos was implemented (Kotake et al. 2003; Takiwaki et al. 2004).

Therefore, we can directly identify the multi-dimensional effects by using this code both in 1D and 2D simulations. On the other hand, the spherical coordinates have a disadvantage for the CFL condition because the length of the lateral direction at the center becomes much smaller than the length of the radial direction, which can be written as $r_1 \Delta\theta \sim 0.02r_1(128/N_\theta)$. Here, r_1 , $\Delta\theta$, and N_θ are the mesh width of the radial direction at the center, that of the latitude, and the mesh number of the lateral direction. This implies that the time step of a 2D simulation with this lateral resolution must be shortened by a factor of 50 compared to a 1D simulation. Therefore, in order to perform long-term simulations in spherical coordinates, we should employ some sort of approximation. In this study, the innermost core of ~ 5 km radius is computed in spherical symmetry, similar to what was done in Buras et al. (2006a).

2.2. Neutrino transfer

In this subsection, we describe the scheme of the neutrino transfer used in this study. This scheme is based on the description in Liebendörfer et al. (2009).

We solve the transport equation for neutrino distribution function $f_l(t, r, \mu, E)$ depending on the time t , radius r , and the momentum phase space spanned by the angle cosine μ , of the neutrino propagation direction with respect to the radius, and the neutrino energy E . In this calculation, we include two neutrino species ($l = \nu_e, \bar{\nu}_e$). We divide the distribution function of neutrinos into two parts as

$$f_l = f_l^t + f_l^s, \quad (5)$$

where f^t is an isotropic distribution function of trapped particles and f^s is a distribution function of streaming particles, representing neutrinos of a given species and energy which find the local zone opaque or transparent, respectively. We solve each component separately as

$$D(f_l^t) = j_l - (j_l + \chi_l)f_l^t - \Sigma_l, \quad (6)$$

$$D(f_l^s) = -(j_l + \chi_l)f_l^s + \Sigma_l, \quad (7)$$

where $D()$ is an operator describing particle propagation, j is a particle emissivity, χ is a particle absorptivity, and Σ is the *diffusion source*, which converts trapped particles into streaming particles and vice versa. In this approximation, Σ is determined by the diffusion limit (see Liebendörfer et al. 2009 for detail). Weak interactions are implemented as described in Bruenn (1985). We assume that the spectrum of f^t is thermal and treat trapped particles as a fluid element. We characterize the thermal equilibrium by a particle number fraction, Y^t , and a particle mean specific energy, Z^t ,

$$Y_l^t = \frac{m_b}{\rho} \frac{4\pi}{(hc)^3} \int f_l^t \epsilon_\nu^2 d\epsilon_\nu, \quad (8)$$

$$Z_l^t = \frac{m_b}{\rho} \frac{4\pi}{(hc)^3} \int f_l^t \epsilon_\nu^3 d\epsilon_\nu, \quad (9)$$

where m_b is the baryon mass, ρ is the baryon density, h is the Planck constant, c is the speed of light, and ϵ_ν is the energy of neutrinos. The advection of these values is calculated in the same way as hydrodynamic quantities. Using the net interaction rates, $s_l = j_l - (j_l + \chi_l)(f_l^t + f_l^s)$, between matter and neutrinos, we can

write the following changes of the electron fraction, Y_e and the internal energy, e :

$$\frac{\partial Y_e}{\partial t} = -\frac{m_b}{\rho} \frac{4\pi c^2}{(hc)^3} \int (s_{\nu_e} - s_{\bar{\nu}_e}) \epsilon_\nu^2 d\epsilon_\nu, \quad (10)$$

$$\frac{\partial e}{\partial t} = -\frac{m_b}{\rho} \frac{4\pi c^2}{(hc)^3} \int (s_{\nu_e} + s_{\bar{\nu}_e}) \epsilon_\nu^3 d\epsilon_\nu. \quad (11)$$

The changes of the electron fraction and specific internal energy feed back the emissivity and absorptivity into Eq. (6), so that we should find the consistent solution by iterating Eqs.(6), (10), and (11). Once the consistent solution has been found, Eq. (6) gives the updated distribution function and specific energy of the trapped particles, which leads to updated Y_l and Z_l values by Eqs. (8) and (9).

2.3. Equation of State

The equation of state (EOS) in supernova simulations needs to handle a large variety of thermodynamic conditions that reflect different nuclear regimes. For temperatures below 0.4 MeV^{10} , time-dependent nuclear reactions are important and the baryon composition is dominated by heavy nuclei. Above this temperature nuclei are in chemical and thermal equilibrium, known as nuclear statistical equilibrium (NSE), where the baryon composition is given by temperature, baryon density and proton-to-baryon ratio (or equivalently the electron fraction in the absence of, e.g., muons). At high densities, typically above normal nuclear matter density, the transition to a state of matter composed of deconfined quarks may be possible. In addition to the baryons (or quarks), a gas of degenerate and possibly relativistic electrons is present. Also (non-degenerate) positrons and photons must be taken into account.

In this study we employ in supernova simulations the two standard EOS for matter in NSE, the Lattimer & Swesty (1991) EOS (LS) and the Shen et al. (1998) EOS (SHEN). LS is based on the incompressible liquid drop model for nuclei, combined with dripped nucleons. The transition to uniform nuclear matter is calculated via a Maxwell phase transition. Contributions from electrons/positrons and photons are taken into account intrinsically. LS has a symmetry energy of 29.3 MeV . Three different values of the incompressibility parameter are available, $K = 180 \text{ MeV}$ (LS180), 220 MeV (LS200), and 375 MeV (LS375). With these one obtains maximum neutron star masses of $\sim 1.8 M_\odot$ (LS180), $\sim 2.0 M_\odot$ (LS200), $\sim 2.7 M_\odot$ (LS375) (see O'Connor & Ott 2011).

SHEN gives only contributions for baryons valid for matter in NSE. It is based on the relativistic mean field theory and the Thomas-Fermi approximation for the description of heavy nuclei. The symmetry energy and the incompressibility are 36.9 MeV and $K = 281 \text{ MeV}$, respectively. It results in a maximum neutron star mass of $\sim 2.2 M_\odot$ (see O'Connor & Ott 2011; Kiuchi & Kotake 2008).

Although LS180 fails to fulfill the recent neutron-star mass constraint from Demorest et al. (2010) of $1.97 \pm$

¹⁰ Although the threshold temperature is slightly higher (around $0.5\text{--}0.8 \text{ MeV}$, depending on density and isospin asymmetry), we have tested also the higher flash temperatures and found no significant difference.

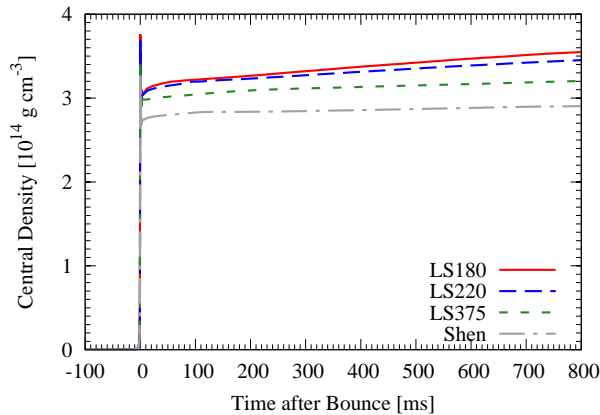


Figure 1. Evolution of the central density, comparing the different EOS under investigation (LS180: red solid line, LS220: blue dashed line, LS375: green dotted line, and SHEN: gray dot-dashed line).

$0.05M_{\odot}$, we nevertheless include it in our EOS comparison study here because it is widely used and because of its similarity to LS220, which does fulfill the Demorest *et al.* constraint.

There are only few experimental constraints on high-density and finite-temperature nuclear EOS. For zero-temperature symmetric nuclear matter, composed of equal numbers of protons and neutrons, the symmetry energy can be well determined. Moreover, recent constraints from nuclear theory, experiments and observations predict a symmetry energy between 31–33.6 MeV with a density gradient between 49.1 and 80 MeV (see Lattimer & Lim 2012). These parameters produce cold neutron star radii between 11–12 km, in agreement with the results of recent efforts to consistently include three-body forces based on low-energy chiral perturbation theory (see, e.g., Steiner et al. 2010; Hebeler et al. 2010). Heavy-ion collision experiments can only hardly be used to constrain the supernova EOS, because the conditions in the collisions are rather isospin-symmetric such that they only cover slightly neutron-rich conditions where $Y_e \simeq 0.485$. But matter in supernova interiors can be extremely neutron rich with $Y_e = 0.01$ – 0.3 . Furthermore, the incompressibility constraint of $200 \text{ MeV} \lesssim K \lesssim 300 \text{ MeV}$ is still weak.

In this paper, we investigate the impact of the EOS on the dynamics of core-collapse supernovae in 1D and 2D simulations. Since the employed EOS cover a wide range of nuclear parameters, we can identify the systematic features that are related to the different EOS.

3. SIMULATIONS IN SPHERICAL SYMMETRY

In the following subsections we compare results obtained in simulations using the four EOS which were discussed in §2.3. We use a $15 M_{\odot}$ progenitor from Woosley & Weaver (1995). We will start with spherically symmetric simulations focusing on the differences between the different LS EOS. Further below, we will also discuss results obtained using SHEN.

The supernova evolution can be separated into the following phases; core collapse, bounce, prompt shock propagation, neutrino burst, and accretion phase (Kotake et al. 2006; Janka et al. 2007). Note that for the post-bounce times considered, explosions could not be obtained in spherical symmetry (see Suwa et al. 2010,

2011, for more details).

3.1. Comparison between different LS EOS

Figure 1 shows the time evolutions of the central density. Because of the difference of the incompressibility K (large K implies a stiff EOS for otherwise identical nuclear parameters), LS180 (red solid line) results in the highest central density, while LS375 (green dotted line) corresponds to the lowest. However, the central density differences between these EOS is $\lesssim 10\%$. Since LS220 exhibits almost identical features as LS180 during the post-bounce phase up to about 500 ms and because LS180 has been used in many previous publications of supernova simulations, we mainly compare LS180 and LS375 in the following. Figure 2, shows the radial bounce profiles of velocity, Y_e , temperature and entropy per baryon as a function of the enclosed mass. The slightly different temperatures obtained right behind the shock and at the very center for the different LS EOS, are due to the different incompressibilities. Highest (lowest) temperatures behind the shock, as well as lowest (highest) temperatures at the stellar core, are reached using LS375 (LS180) (see Figure 2). Moreover, the lowest (highest) Y_e is obtained using LS375 (LS180). However, the differences obtained are small and all LS EOS have very similar profiles. Thus, despite the difference of the central density, the structures of the inner cores at bounce are very similar for all LS EOS, especially the mass enclosed inside the bounce shock and hence the energetics of the bounce shock is practically the same.

All LS EOS show a similar shock evolution post bounce up to about 200 ms post bounce, expanding to $\sim 250 \text{ km}$. After that, the shocks stall and turn into standing accretion shocks. After about $\sim 200 \text{ ms}$ post bounce, LS375 has a larger shock radius than LS180 and LS220 (see Figure 3(a)).

3.2. Comparison between LS and SHEN EOS

SHEN exhibits a significantly lower central density compared to LS375 which is at first view counter-intuitive because SHEN has a lower incompressibility ($K = 281 \text{ MeV}$) than LS375 ($K = 375 \text{ MeV}$). This aspect can be related to the larger adiabatic index of SHEN at high densities around $\approx 2 \times 10^{14} \text{ g cm}^{-3}$. It means that there are regimes where curves of constant entropy per baryon in a $\rho - p$ diagram have a steeper gradient for SHEN. Figure 4 shows the pressure as a function of the density for the employed EOS, at fixed entropy per baryon of $1 k_B$ and electron fraction of $Y_e = 0.3$. Only at very high densities, $\gtrsim 3 \times 10^{14} \text{ g cm}^{-3}$, LS375 has a steeper density gradient and becomes stiffer than SHEN, mainly due to the higher K . This example illustrates that neither incompressibility nor symmetry energy alone determine the nuclear properties of the EOS. It is rather the entire ensemble of nuclear parameters, and in particular also the gradients of the incompressibility and symmetry energy, which determine the EOS and hence the possible outcome of dynamical simulations.

At core bounce and shortly after, the shock wave propagates at high densities, where the highest pressure of SHEN results in the largest shock radius. Later during the post-bounce evolution, the bounce shock propagates towards lower densities on the order of 10^9 – $10^{13} \text{ g cm}^{-3}$, where all EOS are very similar (Figure 3(a)).

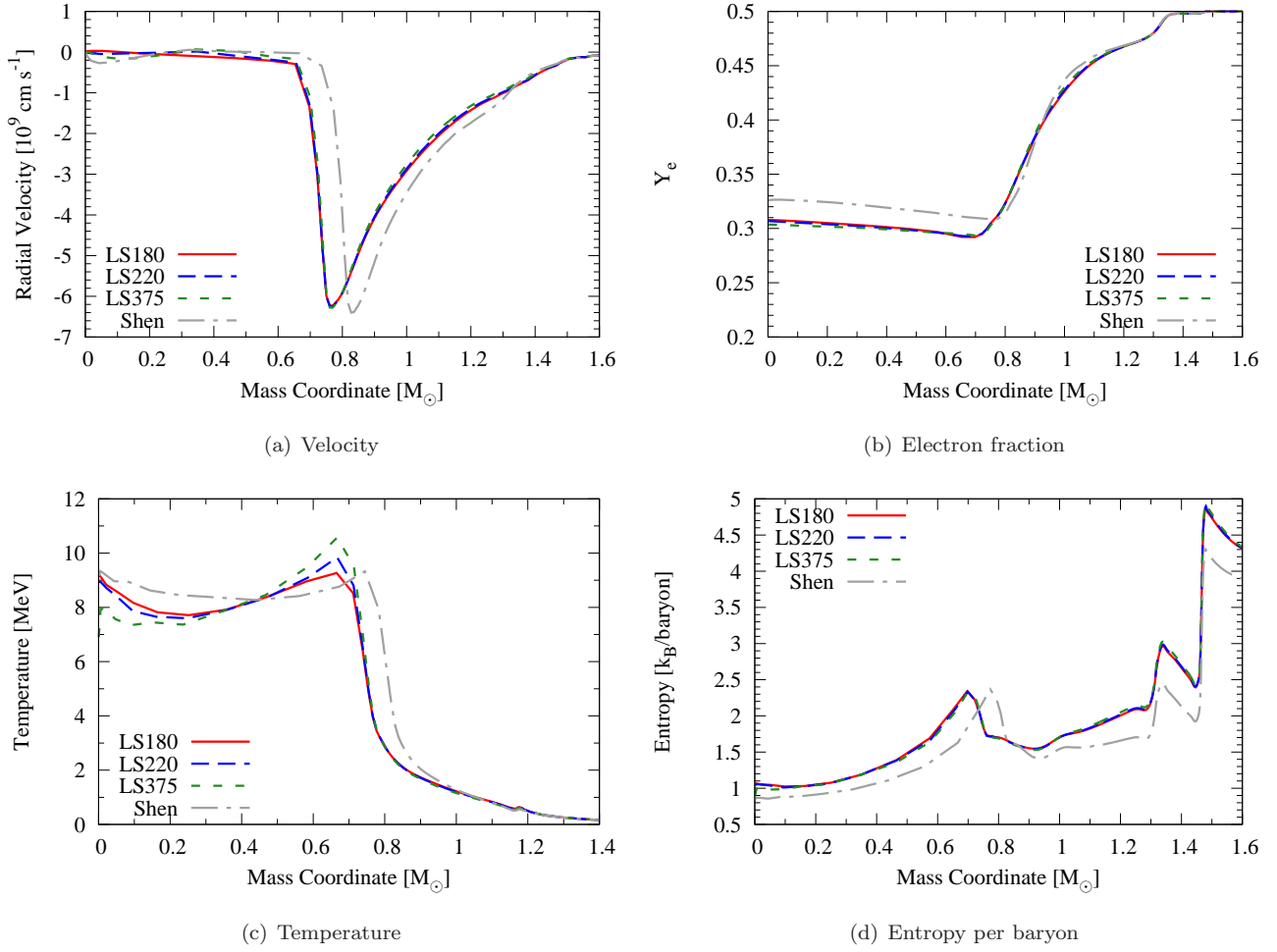


Figure 2. Radial bounce profiles as a function of the enclosed baryon mass. The velocity jump (at $\sim 0.7 M_\odot$ for LS EOS and $\sim 0.8 M_\odot$ for SHEN) mark the edge of the inner core, above which the accretion flow is supersonic. The inner core at this time is not swept by the shock wave so that the inner core maintains its low entropy.

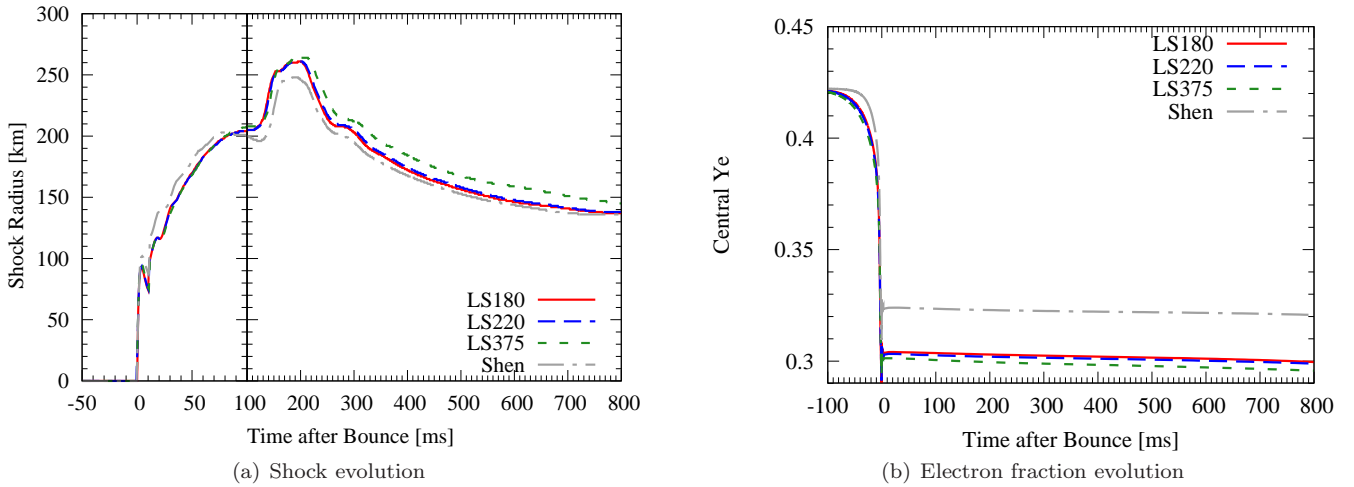


Figure 3. The left panel shows the evolution of the shock radius. Note that the time axis uses two different scales to clearly show the early post-bounce phase. The right panel shows the evolution of the central electron fraction for the different EOS under investigation.

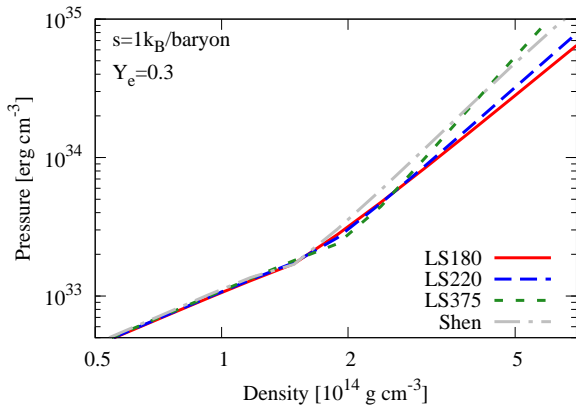


Figure 4. The pressure as function of the density for the case of $s=1k_B/\text{baryon}$ and $Y_e=0.3$. These conditions correspond to the most central part of the collapsing core where the neutrinos are completely trapped. Above nuclear density ($\approx 3 \times 10^{14} \text{ g cm}^{-3}$) the difference between the EOS is significant.

Bounce conditions of selected quantities are illustrated in Figure 2 in comparison to the LS EOS. The most important difference is the larger mass enclosed inside the core at bounce for SHEN. This difference cannot only be related to the incompressibility. More relevant is the symmetry energy, which mainly affects the evolution of the electron fraction Y_e . Note that the dominant contributions to the pressure are given by the degenerate electron gas during the core-collapse phase, while after bounce the dominating contributions come from nucleons in the highly dissociated regime behind the shock wave. Figure 3(b) shows the evolution of the central Y_e for the different EOS. Y_e is very similar for all LS EOS. But for SHEN, Y_e is significantly larger than for any LS EOS, already during core collapse. At bounce this difference results in $Y_e \simeq 0.32$ for SHEN and $Y_e \simeq 0.3$ for LS. It indicates a slower iron-core deleptonization during collapse and explains the larger core mass at bounce of about $0.8 M_\odot$ for SHEN. The models based on LS EOS result in core masses of about $0.7 M_\odot$. The different shock positions at bounce relate to these differences in the structures of the core (see the temperature and Y_e profiles in Figure 2) and hence reflect the different shock energetics during the initial propagation. Note the lower central entropy per baryon for SHEN in comparison to LS, which is mainly due to the well known problem of the interactive LS EOS implementation, producing a systematically too low fraction of α -particles at low density. We did not correct for this in the current study. Note also the lower entropy per baryon for SHEN outside about $1.5 M_\odot$. It is related to the different non-NSE treatments, based on the ideal Si-gas approximation, in LS and SHEN. Our findings are consistent with previous studies comparing LS and SHEN, see e.g. Sumiyoshi et al. (2005) and Hempel et al. (2012). It is also worth mentioning that the incorrect alpha-particle fraction of LS EOS has a negligible impact on neutrino heating/cooling in the post-shock regions because all nuclei (including alpha-particles) dissociate into free nucleons (e.g., panel (e) of Figure 7 in Hempel et al. 2012). Moreover in the preshock regions, inelastic neutrino scattering of light nuclei, which was proposed to preheat material there (Haxton 1988, see Ohnishi et al. 2007 for col-

lective references therein), has recently been shown to have negligible impact on assisting the neutrino-driven explosions (Langanke et al. 2008).

Note that the inner-core mass of 0.7 and $0.8 M_\odot$ for the enclosed baryon mass at bounce are too high values that are due to the approximations employed in our simulations. We omit neutrino scattering on electrons/positrons and general-relativistic effects, which lead to smaller inner core masses at bounce (see Liebendörfer et al. 2001; Thompson et al. 2003). In addition, we use the electron-capture rates from Bruenn (1985), also for heavy nuclei, which assume a single representative nucleus with average charge and mass. Improved electron-capture rates on heavy nuclei from Langanke et al. (2003), which are based on the NSE distribution of heavy nuclei, also lead to smaller core masses at bounce (see Hix et al. 2003 and Janka et al. 2007 for details).

These size differences of the inner core mass lead to different shock evolutions. Due to the larger inner core, SHEN initially shows a slightly more rapid expansion of the shock wave. However, ~ 50 ms after bounce the shock contracts faster towards the PNS for SHEN than for any LS EOS. The reason is a larger energy loss with SHEN when the shock propagates with its larger energy across the neutrinospheres, from where the deleptonization burst is released. This effect can also be seen in the luminosities. Before the explosion is launched, the electron (anti)neutrino luminosity is determined by mass accretion during the post-bounce evolution. With the accretion rate \dot{M} and an enclosed mass M at the neutrinospheres R_ν one obtains the accretion luminosity as

$$L_{\text{acc}} \simeq 8 \times 10^{52} \left(\frac{M}{1.5 M_\odot} \right) \left(\frac{50 \text{ km}}{R_\nu} \right) \left(\frac{\dot{M}}{1 M_\odot \text{ s}^{-1}} \right) \text{ erg s}^{-1}. \quad (12)$$

Figure 5 shows the post-bounce evolution of this quantity for the different EOS under investigation. The highest mass accretion rates for SHEN explain the highest luminosities for SHEN until about 150 ms post bounce, in comparison to the LS EOS. During the later post-bounce evolution, the mass accretion rates at the neutrinospheres become very similar for all EOS considered. Only small differences can be identified with slightly lower luminosities for the stiffer LS375 and SHEN on the one hand, and slightly higher luminosities for the softer LS180 and LS220 on the other hand.

4. RESULTS OF 2D SIMULATIONS

In this section, we present our results of 2D simulations. We perform 2D simulations for LS180, LS375, and SHEN. Since LS220 shows almost the same features as LS180 as seen in the previous section, we do not include it in this section.

4.1. Comparison between 1D and 2D using LS180

First of all, we compare the results of spherically symmetric and axially symmetric simulations using LS180. For the 2D simulation we obtain a weak explosion, corresponding to the so-called “passive expansion” (Buras et al. 2006a; Suwa et al. 2010), in which the rate of mass accretion through the shock is larger than that of mass-ejection, so that the mass of the

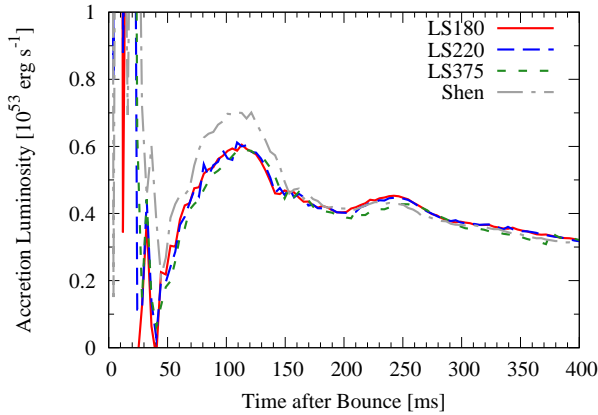


Figure 5. Post-bounce evolution of the accretion luminosity for the EOS under investigation.

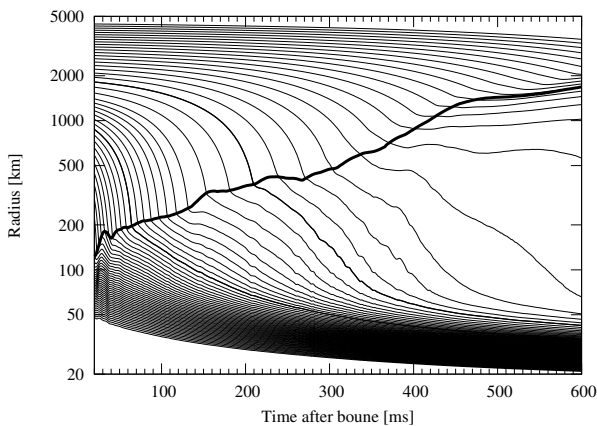


Figure 6. The mass trajectory as a function of time after the bounce for 2D simulation of $15 M_{\odot}$ with LS180. The thick black line represents the angle-averaged shock radius. The grey lines show the mass from 1.0 to $1.7 M_{\odot}$ at intervals of $0.01 M_{\odot}$. Two thin black lines indicate 1.4 and $1.5 M_{\odot}$, respectively.

central PNS is still increasing after the onset of shock expansion¹¹. On average, only the continuous shock expansion to larger radii is obtained with yet no significant matter outflow (see Figure 6) for the simulation times considered. The shock expansion is an effect of the accumulation of hot matter in combination with a decreasing ram pressure of the material ahead of the shock. The ram pressure decreases because of a decreasing accretion rate and the propagation of the shock to larger radii where the gravitational potential is less deep.

In Figure 7 we show the entropy distribution at the north pole (top panel) and the south pole (bottom panel) for the 2D simulation. The deviation from a spherically symmetric distribution becomes prominent after about 20 ms post bounce when convection starts behind the shock and shock wave oscillations start to introduce substantial differences of the shock position at the north and south poles. The standing accretion shock instability (SASI) drives such shock oscillations on a longer timescale on the order of several 100 ms. Until about 300 ms post bounce, the standing accretion shock expands only slowly to several 100 km. After that, the

shock expands faster and reaches about 1000 km at the north pole and 2000 km at the south pole at about 500 ms post bounce. We will return to the origin of the increasing difference between north- and south-pole evolution further below. Here, we will discuss the entropy distribution obtained in comparison with the spherically symmetric simulation.

Figure 8 shows the radial entropy distribution obtained in the 2D simulation (red and blue points) and the 1D simulation (green line), at 50 ms, 100 ms, 200 ms, and 300 ms after bounce. In general, the entropy spreads over a wider range in 2D than in 1D, because of the convective activity between the shock and the gain radius (i.e., the region where neutrino heating exceeds cooling). The higher entropy in 2D is realized by more efficient neutrino heating, in comparison to 1D (Herant et al. 1994; Burrows et al. 1995; Janka & Mueller 1996; Murphy & Burrows 2008). Note that at late times, shown in the bottom panels of Figure 8, once maximum entropy ($s \sim 13 k_B$ per baryon in the bottom left panel and 16 in the bottom right panel) is obtained, matter at small radii (~ 100 km) does not gain additional entropy/energy as it floats to larger radii. This is related to the convection which drives matter from the gain radius, where the heating is maximum, to larger radii, where the heating is less efficient. Thus, the specific entropy is limited to the value at the gain radius. This is illustrated in Figure 8, where red points represent matter with positive radial velocity (i.e., escaping) that have high entropy, while blue points (accreting material) have low entropy. For comparison, we show the weak equilibrium entropy for the 1D simulation (green dotted line), that would be achieved by infinitely-long exposure of matter to the prevailing neutrino abundances and spectra. We construct this line by keeping hydrodynamic quantities unchanged and solve the neutrino emission and captures until equilibrium is almost achieved (see also Liebendörfer et al. 2004). The region where the entropy is below this line has the potential to be heated by neutrino radiation up to the equilibrium entropy, while the region above this line is dominated by neutrino cooling. In 1D the entropy beyond the gain radius (corresponding to the radius of the maximum entropy, $r \sim 100$ km) decreases with increasing radius, while the equilibrium entropy increases continuously with radius. The difference between the obtained entropy in the simulations and the equilibrium entropy is caused by the insufficient time for the heating, i.e., too short advection timescale compared to the neutrino heating timescale (see the discussion in Buras et al. 2006a for instance). Thus, the region above the gain radius has room to absorb more neutrinos in multi-dimensional simulations. The convective motion continuously exchanges equilibrated matter from the gain radius by below-equilibrium matter from layers that are too distant for efficient neutrino heating. This exchange of matter by fluid instabilities enables continued neutrino heating at the gain radius in combination with the steady distribution of the heated matter to the outer layers (Herant et al. 1994). Moreover, the convective motion is expected to prolong the advection timescale and lead to more effective neutrino heating. In summary, the higher entropy obtained in 2D simulation is due to the presence of convection and SASI in the gain region. However, even in 2D the advection

¹¹ Note that the post-shock material have partly positive velocities (e.g., Figure 9(a)).

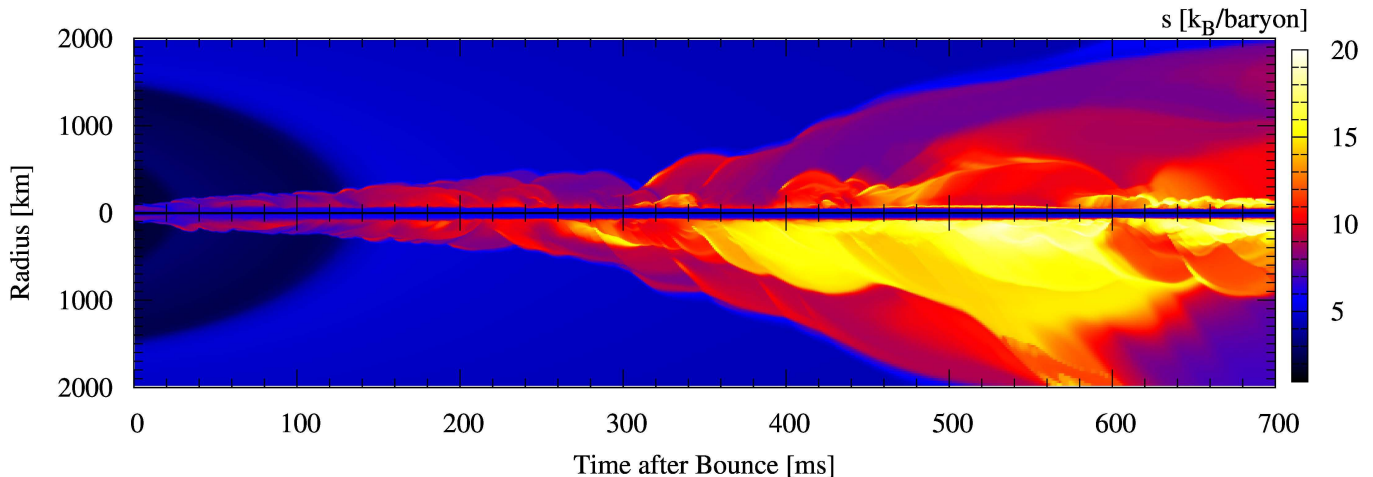


Figure 7. Post-bounce evolution of the entropy distribution, illustrated in a space-time diagram. The top and bottom panels correspond to the northern pole and southern pole, respectively. The high-entropy region (red or yellow) shows the post shock layer. The shock wave oscillation produced by SASI and convective motion is apparent. The shock wave at the southern pole reaches a distance of 2000 km from the center earlier than at the north pole, corresponding to the existence of a $\ell = 1$ mode of the SASI.

timescale is finite so that the equilibrium entropy is not realized. Part of the material just below the gain radius maintains a higher entropy than the equilibrium value because of the overshooting of high entropy matter by convective motion. This phenomenon disappears deeper inside the gain region ($r \lesssim 50$ km) because the weak interaction rates at high density become large so that the entropy coincides with the value determined by weak and thermal equilibrium.

In Figure 9(a) we show the time snapshot of the entropy distribution at 400 ms after bounce. The left panel shows the central part and the right panel is a wider view. In the left panel, red arrows indicate infalling matter (negative radial velocity) and blue arrows outstreaming matter (positive radial velocity). An important structure becomes visible: low-entropy infalling matter (“downflow”, see Herant et al. 1992; Burrows et al. 1995; Janka & Mueller 1996) is accreting onto the central PNS as indicated by the green area in Figure 9(a) (left panel). On the right-hand-side panel of Figure 9(a), a triple shock point is seen to be located in the northern hemisphere near the position of (600 km, 200 km). If one now compares with the left-hand-side panel of Fig 9a, one recognizes that the cold downflow through the triple point advects directly to the surface of the PNS. Hence, the cold downflow stems from large distances, between 500 and 1000 km, and reaches down to the PNS surface. It exists as a quasi-stationary structure and supplies energy and momentum to the PNS in an asymmetric way. The momentum is reflected at the surface of the PNS and becomes visible as a pressure wave in Figure 13, which pushes the shock wave to larger radii and increases the amplitude of the SASI by the so-called “advective-acoustic cycle” (Foglizzo et al. 2007). This feedback cycle stands at the origin of the anisotropic shock evolution between north and south poles which significantly promotes the shock expansion reaching larger radii at the south pole.

The IDSA neutrino transport scheme employed in this study permits an estimate of the proton-to-baryon ratio of the possibly ejected material from the PNS surface. In Figure 10 we show the Y_e distribution at 400 ms

post bounce. Infalling material at large radii, dominated by heavy nuclei, starts with the progenitor value of $Y_e \simeq 0.5$. The electron fraction then decreases continuously due to electron captures as the material is compressed while accreting onto the PNS surface, where Y_e finally reaches values as low as $\simeq 0.05$ – 0.2 . However, the high-entropy region, which corresponds to expanding matter, experiences a continuous flux of neutrinos that stream off the PNS surface. There, in the presence of similar electron neutrino and antineutrino luminosities, and small average energy differences below 4 MeV between ν_e and $\bar{\nu}_e$, matter becomes proton rich. Similar results have been reported in previous studies of massive star explosions that employ sophisticated neutrino transport (e.g., Liebendörfer et al. 2001; Buras et al. 2006b; Fröhlich et al. 2006; Pruet et al. 2006; Wanaajo 2006; Fischer et al. 2010).

In contrast to spherically symmetric models, multi-dimensional models permit mass outflow alongside accreting matter and hence, e.g., mixing with the surrounding material. Mixing opens interesting aspects for the chemical evolution of explosion models which cannot be obtained using 1D models. This has been discussed at the example of the $8.8 M_\odot$ O-Ne-Mg-core explosion model in Wanaajo et al. (2011) by comparing 1D and 2D results. Neutron-rich conditions were obtained in both cases due to the extremely fast initial expansion of the ejecta. However, while only slightly neutron-rich conditions could be obtained in 1D, mushroom-like and more neutron-rich pockets developed in 2D.

4.2. Comparison of 2D models with different EOS

Here, we compare the 2D results for the $15 M_\odot$ progenitor using the different EOS, i.e., LS180, LS375, and SHEN. Figure 11 shows the shock-radius evolution for each model. Each of which has three lines, corresponding to maximum, angular averaged and minimum shock radius (from top to bottom). Note that the minimum shock radius often coincides with the position of the triple point of the shock, which is the starting point of the cold downflow (see Figure 9(a)). In Figure 11, we can see that LS180 and LS375 (red solid lines and green dotted lines) show similar trajectories. There is a gradual expansion

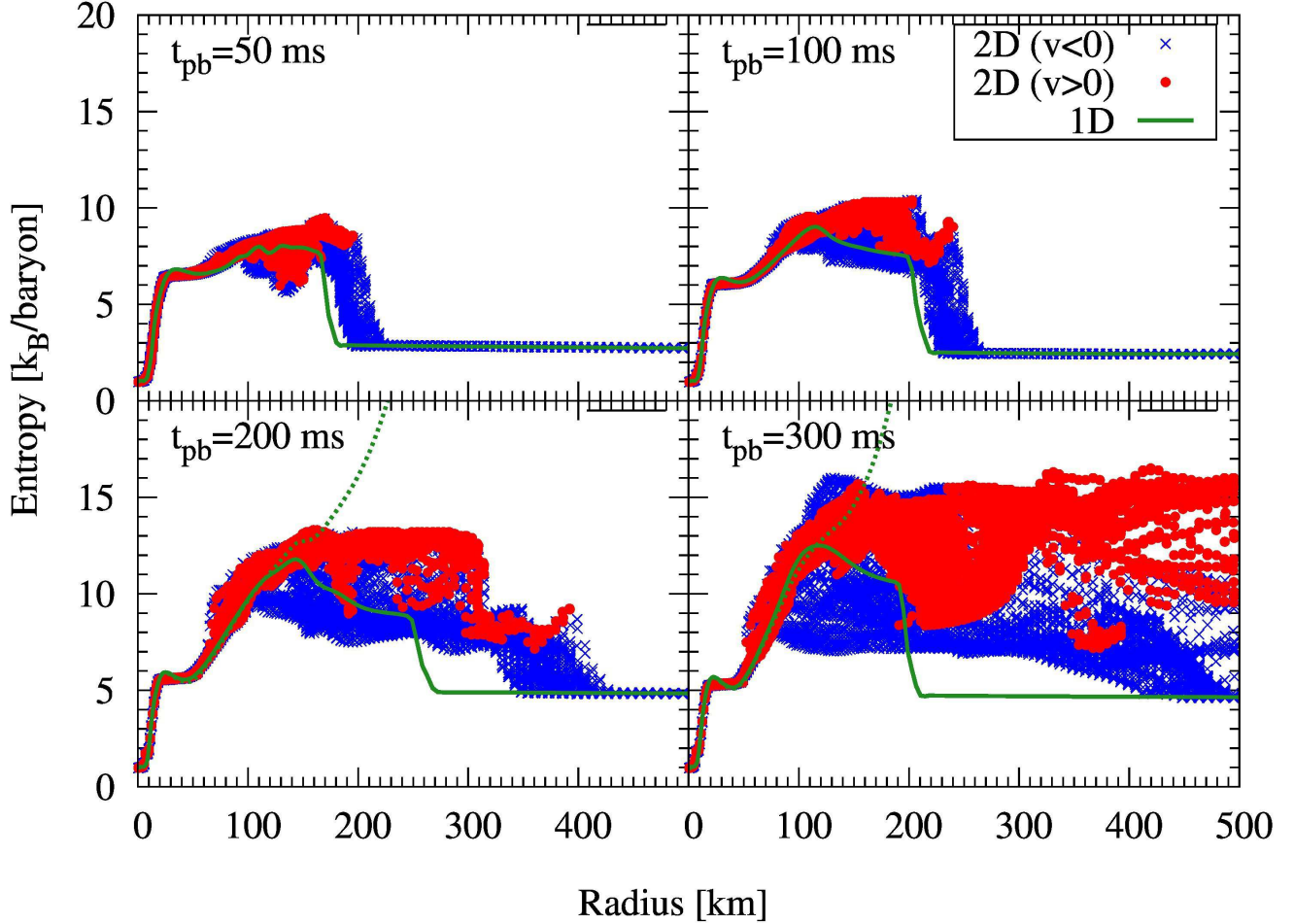


Figure 8. Radial entropy distribution of the simulations with LS180. Red and blue points represent result of the 2D simulation, the green solid line corresponds to the 1D results. In addition, the green dotted line shows the entropy in weak equilibrium that would be achieved by infinitely-long exposure of the matter to the prevailing neutrino abundances and spectra.

phase during the post-bounce time $t_{\text{pb}} \lesssim 200\text{--}300$ ms, where the maximum shock radii grow to about 500 km. While afterwards, they grow more rapidly in both models and reach about 2000 km for LS180 and 1800 km for LS375 at 500 ms post bounce. These two models show no phase of shock retraction. For the 2D simulation using SHEN, on the other hand, the shock wave does not enter this second phase of fast shock expansion even at late times (see Figure 11).

Before analyzing the origin of this observed difference in the shock evolution between SHEN and LS180 further, a comment regarding the likelihood to find explosions in our models seems in order: At the time the 2D simulations are stopped, the “diagnosing explosion energy”, as defined in Suwa et al. 2010, achieves $\sim 10^{50}$ erg in both LS EOS cases, while explosions for the 2D simulations using SHEN are unlikely to occur. LS180 has been applied in axially symmetric simulations of the same $15 M_{\odot}$ progenitor in Marek & Janka (2009), where the average shock radius was found to oscillate around 200 km for several 100 ms until it eventually starts to expand at about 600 ms post bounce, i.e. much later than in our simulations. The fast and continuous shock expansion to increasingly larger radii for our LS180 simulation is

likely due to the omission of the continuous energy loss by the emission of heavy lepton neutrinos, and possibly the neglect of general relativistic effects in the gravitational potential. Coming back to the discussion of the differences between LS180 and SHEN, we will analyze in the following the two different aspects of (a) neutrino heating/cooling, and (b) subsequent convective activity.

Figure 12 illustrates the evolution of the neutrino luminosities and average energies in 1D (thin lines) and 2D (thick lines), comparing LS180 (red solid line) and SHEN (grey dot-dashed line), for electron neutrinos (left panel) and antineutrinos (right panel), respectively. Note the rapid variations in the luminosities on a millisecond timescale, which are due to the convective activity in the vicinity of the PNS (e.g., Marek et al. 2009). At first, the luminosities (sampled at the equator) are in qualitative agreement with the results obtained in spherical symmetry. The mean neutrino energies in the 2D models are slightly, but systematically, smaller than in the 1D models. When the standing shock starts to propagate faster to increasingly larger radii in 2D, i.e. at about 350 ms post bounce for LS180, the ν_e and $\bar{\nu}_e$ energies cease to rise and stay nearly constant (see Figs. 12(a) and 12(b)). Furthermore, the luminosities decrease rapidly and de-

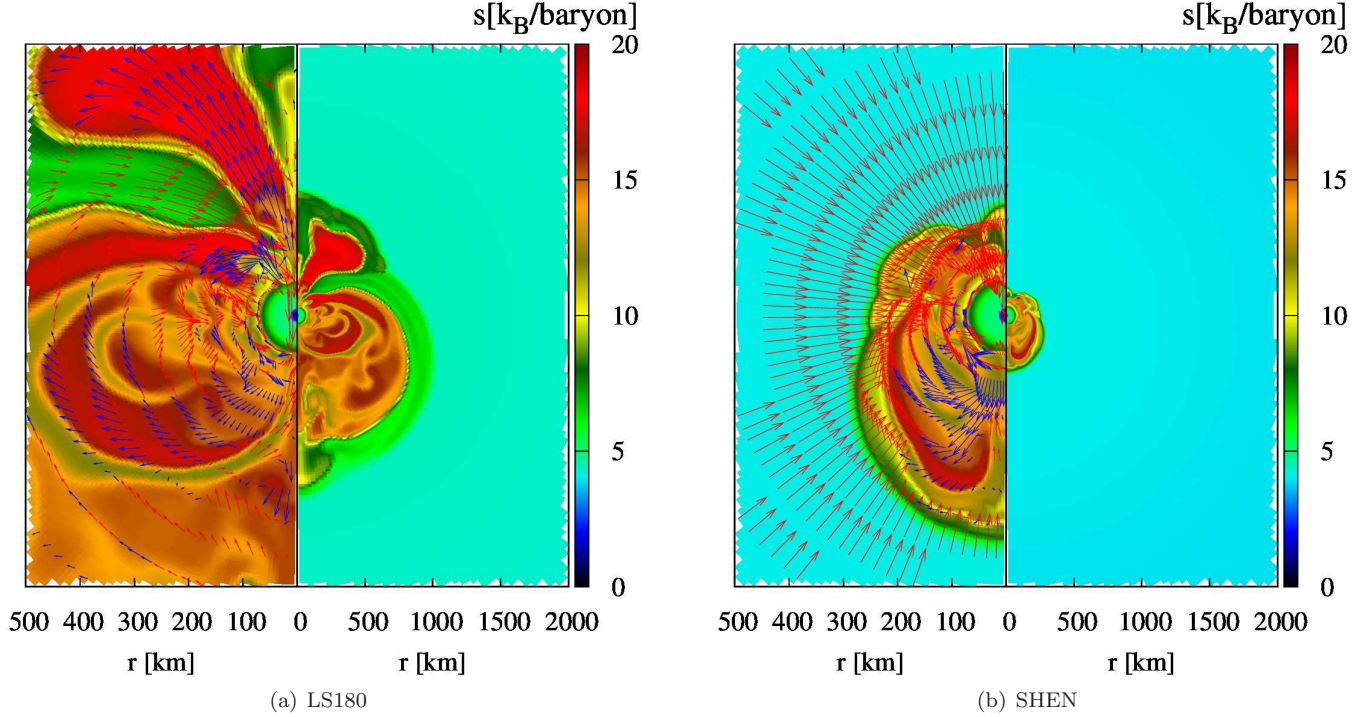


Figure 9. Snapshot at 400 ms post bounce of the entropy distributions comparing LS180 and SHEN. Red and blue arrows show the in- and outflowing velocity fields, respectively. The left panel shows the inner part while the right panel is a wider view. The shock wave is strongly deformed due to SASI activity and turbulent matter motion induced by convection. In the left panel we can see a cold downflow of matter that comes from the northern hemisphere, which activates a pressure wave in the southern hemisphere (see text for detail). This feature originates from the triple point of the shock wave that is shown in the northern hemisphere of the right panel.

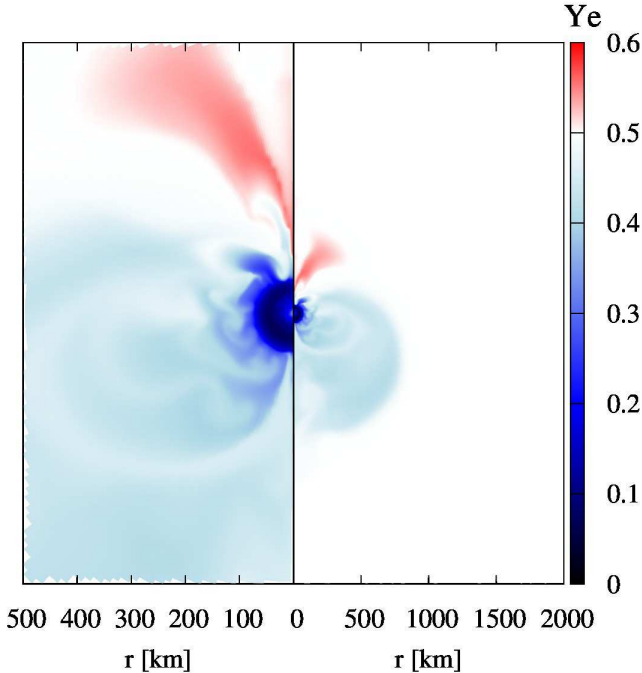


Figure 10. Y_e distribution for the simulation using LS180 at 400 ms post bounce. Escaping material exhibits proton-rich conditions with $Y_e > 0.5$, while infalling material becomes neutron rich due to electron captures.

viate from the 1D results (see Figs. 12(c) and 12(d)). This phenomenon is more prominent for ν_e , whose neutrinosphere is located at lower densities than those of $\bar{\nu}_e$.

The LS180 and SHEN EOS lead to different central

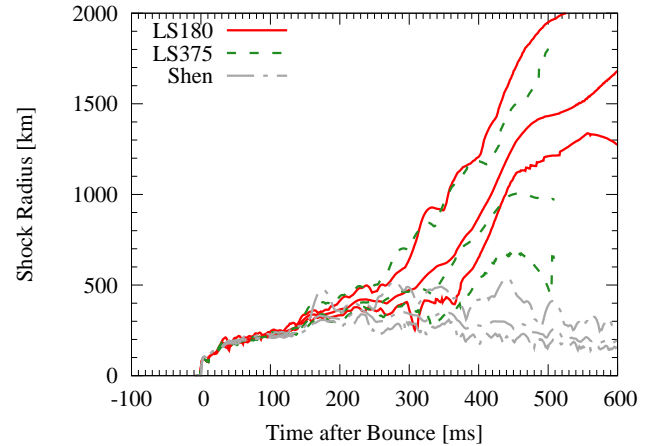


Figure 11. Shock trajectories for the 2D simulations using the different EOS LS180 (red-solid lines), LS375 (green-dotted lines), and SHEN (gray dot-dashed lines). We show three lines for each model, which correspond to the maximum shock radius, the angular averaged one, and the minimum radius, from top to bottom.

configurations during the post-bounce evolution, as a result of the different PNS contraction behaviors. In comparison to the stiffer SHEN EOS, the soft LS180 EOS results in a more compact PNS with higher central density and a steeper density gradient at its surface. The impact of different PNS structures on the properties of emitted neutrinos has been discussed in many places of the literature (see, e.g., Hempel et al. 2012). A direct consequence of the different PNS structures is the different evolution of the neutrino luminosities (see Figs. 12(c) and 12(d)). In 1D, the neutrino luminosi-

ties (thin lines) become slightly smaller for SHEN compared to LS180. However, the difference between SHEN and LS180 is much smaller than what has been found in Sumiyoshi et al. (2005); Fischer et al. (2009). The reason might be that our PNS is less compact due to the neglect of heavy-lepton neutrinos and general relativistic gravity. As the shock for LS180 in the 2D simulations starts to expand continuously after about 350 ms post bounce, we will focus on post-bounce times before that moment to search for the origin of more efficient neutrino heating in LS180 compared to SHEN. It can be seen in Figs. 12(c) and 12(d) that the ν_e luminosities are rather similar for LS180 and SHEN, while the $\bar{\nu}_e$ luminosities differ considerably during the first 250 ms post bounce. We explain these differences by the fact that the $\bar{\nu}_e$ neutrinospheres are located at higher density where the EOS differences between LS180 and SHEN are larger than at the lower density where the ν_e neutrinospheres are located. The sizeable difference in the $\bar{\nu}_e$ luminosity leads to less efficient heating for SHEN, and consequently to a lower entropy per baryon in the gain region than in the simulations based for LS180 (see Figure 9(b)). How the luminosity decays at later times, as observed here after the onset of the explosion in the simulations using LS180, and as predicted by recent spherically symmetric explosion models, needs to be elaborated by long-term multi-dimensional simulations that cover several seconds after the onset of explosion. This is yet computationally very expensive and beyond the scope of the present study.

In the following paragraph, we will return to aspect (b), which is a comparison of convective activities between our 2D models using SHEN and LS EOS. The left panel of Figure 13 shows the post-bounce evolution of the kinetic energy of the lateral (θ) direction, $\int \rho v_\theta^2/2 dV$, where V is the entire simulation domain. This quantity is zero in spherical symmetry such that non-vanishing values imply a deviation from sphericity. Models based on LS180 and LS375 exhibit a significantly larger amplitude than SHEN for $t_{\text{pb}} \lesssim 50$ ms. This is the so-called prompt convection, which is triggered by the negative entropy gradient left behind the prompt shock as it weakens by dissociation of nuclei and eventually comes to a complete stall by the emission of the deleptonization burst. In the right panel of Figure 13, we show the radial profiles of the root-mean-square of the radial velocity, $(\int v_r^2 \sin \theta d\theta)^{1/2}$. For LS180 (upper part), convective motion is apparent between 30–100 km during the first 50 ms after bounce, which is seen as a yellowish island in the plot. This shows that the convective flows produced by the fluid instabilities advect down to the inner surface of the PNS (white dashed line). The occurrence of this advection-mediated convective motion has been already mentioned in Buras et al. (2006a); Dessart et al. (2006). For SHEN (lower panel of Figure 13(b)), such a behavior is only weakly visible due to the smaller volume of the convectively unstable region. Note that after the convection has ceased, both, LS180 and LS375, still have larger kinetic energy than SHEN.

In order to analyze the evolution of the shock wave, we conduct a mode analysis as follows: The deformation of the shock surface is decomposed into spherical harmonic

components

$$R_s(\theta) = \sum_{\ell=0}^{\infty} a_\ell \sqrt{\frac{2\ell+1}{4\pi}} P_\ell(\cos \theta). \quad (13)$$

Note that due to axisymmetry, only $m = 0$ harmonics are relevant. The coefficients, a_ℓ , can be calculated by the orthogonality of the Legendre polynomials,

$$a_\ell = \frac{2\ell+1}{2} \int_{-1}^1 R_s(\theta) P_\ell(\cos \theta) d \cos \theta. \quad (14)$$

The position of the shock surface, $R_s(\theta)$, is estimated from the isentropic surface of $s = 6k_B$ per baryon.

Figure 14 shows the post-bounce evolution of the low mode ($\ell = 1$ and 2) for LS180 and SHEN. During the early phase ($t_{\text{pb}} \lesssim 100$ ms after bounce), LS180 has a significantly larger amplitude than SHEN. After that the amplitudes are similar in the time window $100 \lesssim t_{\text{pb}} \lesssim 300$ ms. For LS180, the shock wave begins to expand more rapidly at $t_{\text{pb}} \sim 300$ ms, after which the amplitude is decreasing continuously with time. For SHEN, the shock wave continues to oscillate at smaller radii and does not expand. This in turn results in an increasing amplitude. At $t_{\text{pb}} \gtrsim 500$ ms, LS180 shows a dominant $\ell = 1$ mode (red line) due to the expansion of the shock, while SHEN shows a decreasing amplitude because the retracting shock wave is approaching a spherical shape. This corroborates the failed explosion for SHEN. Note that the mode analysis of the shock radius, albeit very helpful to extract the information of SASI modes, serves as a reliable indicator of the explosion only if it is combined with other criteria such as the convention timescale argument regarding the heating/advection timescale and the antesononic condition that we will discuss later in this section.

Next, we discuss the EOS dependence of the SASI activity (acoustic-vorticity cycle). We show the pressure deviation for LS180 and SHEN in Figure 15. It is determined as follows:

$$\frac{\left\{ \frac{1}{2} \int_0^\pi [\mathcal{M}(r, \theta) - \overline{\mathcal{M}}(r)]^2 \sin \theta d\theta \right\}^{1/2}}{\overline{\mathcal{M}}(r)}, \quad (15)$$

where

$$\mathcal{M}(r, \theta) \equiv \rho(r, \theta) v_r^2(r, \theta) + P(r, \theta), \quad (16)$$

$$\overline{\mathcal{M}}(r) \equiv \frac{1}{2} \int_0^\pi \mathcal{M}(r, \theta) \sin \theta d\theta. \quad (17)$$

\mathcal{M} is the total pressure, including the ram pressure of the infalling material. It should assume the same value ahead and behind the shock wave (corresponding to the momentum part of the Rankine-Hugoniot equation). Therefore, \mathcal{M} is a useful quantity to investigate the shock expansion: If \mathcal{M} is greater behind the shock than ahead of the shock, the shock wave propagates outward, and vice versa. Before 100 ms postbounce, the dispersion of \mathcal{M} is small (~ 0.1) (especially for SHEN; see Figure 15). Later, the pressure perturbation increases in the shocked region and the shock wave is pushed outward. For LS180, the pressure perturbation continues to grow after $t_{\text{pb}} \sim 200$ –300 ms and a strong pressure wave transfers momentum to the shock. This phenomenon is absent

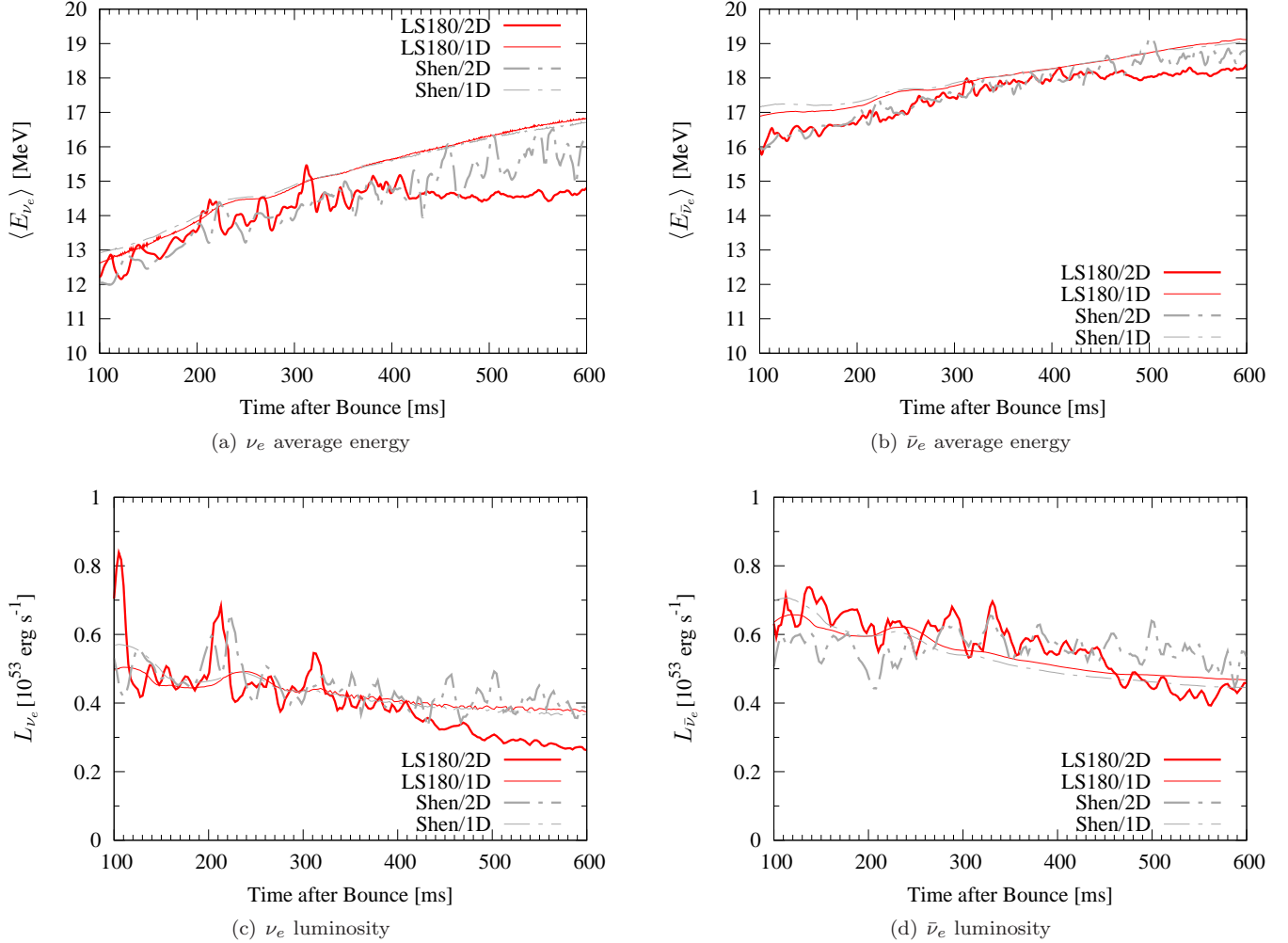


Figure 12. Post-bounce evolution of neutrino mean energies and luminosities, for the 2D simulation using LS180 and SHEN sampled at the equator (thick lines). For comparison, we also show results from the 1D simulation using the same EOS (thin lines).

in the simulations using SHEN. As a consequence in the LS180 model, the pressure behind the shock wave becomes greater than the ram pressure ahead of the shock, so that the shock begins to propagate outward without receding. Note that the pressure wave appears to be produced close to the PNS surface (see the thick dashed lines in Figure 15), where the vorticity is reflected at the steep density gradient (see also the right panel of Figure 13).

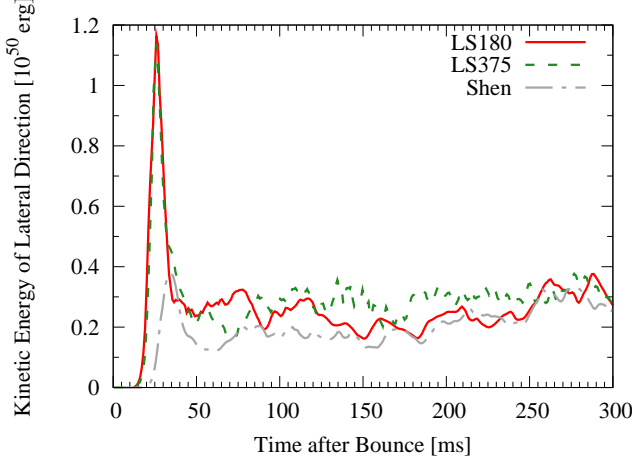
In order to characterize the spatial anisotropy of downflows for the different EOS used, we estimate the following ratio, \mathcal{R} , which is determined by

$$\mathcal{R} \equiv \frac{1}{2} \left(\frac{E_K^N}{E_K^S} + \frac{E_K^S}{E_K^N} \right) - 1, \quad (18)$$

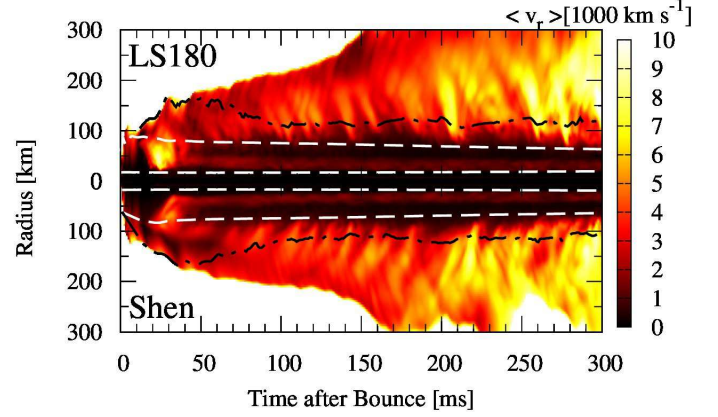
where E_K^N and E_K^S are the kinetic energy accreted from the northern (N) and southern (S) hemispheres, respectively. $E_K = \int \rho v_r^2 / 2 dA$, where the integration extends over the surface of a sphere with a radius of 100 km. In Figure 16(a), we show the post-bounce evolution of \mathcal{R} , comparing LS180, LS375, and SHEN. It implies that LS180 and LS375 have greatly asymmetric mass accretion after 300–400 ms post bounce, while for SHEN the mass-accretion asymmetry is small.

In the following paragraphs, we investigate possible

indicators of the onset of explosion which have been previously explored in the literature. One of those is the mass-weighted average entropy in the gain region, discussed as an indicator of the neutrino-heating efficiency in Murphy & Burrows (2008) and Nordhaus et al. (2010). It has been suggested that exploding models exhibit higher entropy in the gain region prior to the onset of explosion, as a result of more efficient neutrino heating, in comparison to non-exploding models of the same progenitor. Figure 16(b) shows the post-bounce evolution of the average entropy, $\langle s \rangle$, comparing LS180, LS375, and SHEN. In agreement with previous studies, we find that the optimistic simulations, which show a continuous shock expansion to increasingly large radii (LS180, LS375), have higher average entropy than the less-optimistic one (SHEN), until the onset of explosion at about 350 ms for LS180. Once the explosion has been launched, the entropy-growth rate slows down and even decreases as a consequence of a continuous accretion of cold matter from the upwind side. Note that the entropy per baryon will rise again at the moment when mass accretion will turn into mass outflow, such that net neutrino heating establishes at the surface of the PNS. A similar phenomenon has been observed when increasing the dimensionality in simulations of neutrino-driven



(a) Integrated kinetic energy of the lateral direction.



(b) Distribution of the root-mean-square of the radial velocity in a space-time diagram. The top half and bottom half correspond to LS180 and SHEN, respectively.

Figure 13. Post bounce evolution of kinetic energy and root-mean-square of the radial velocity field as indicators for convective activity. In graph (a), both, LS180 (red solid line) and LS375 (green dashed line), exhibit a strong activity, while the activity for SHEN (gray dash-dotted line) is weaker by a factor of ~ 3 during the first 50 ms after bounce. After that, prompt convection vanishes and LS180 and LS375 maintain slightly larger kinetic energy than SHEN. In graph (b), the colored region is the post-shock layer. The black dash-dotted lines indicate the position of the gain radius and the white dashed lines are the radii of $\bar{\rho} = 10^{11}$ (outer) and 10^{13} g cm^{-3} (inner), where $\bar{\rho}$ is the angle averaged density. The advection-mediated convective motion (see text) is apparent for $10^{11} \text{ g cm}^{-3} \lesssim \bar{\rho} \lesssim 10^{13} \text{ g cm}^{-3}$ and $t_{\text{pb}} \lesssim 50$ ms for LS180. After such convective motions vanish, weak continued PNS activity is visible above $\bar{\rho} = 10^{13} \text{ g cm}^{-3}$.

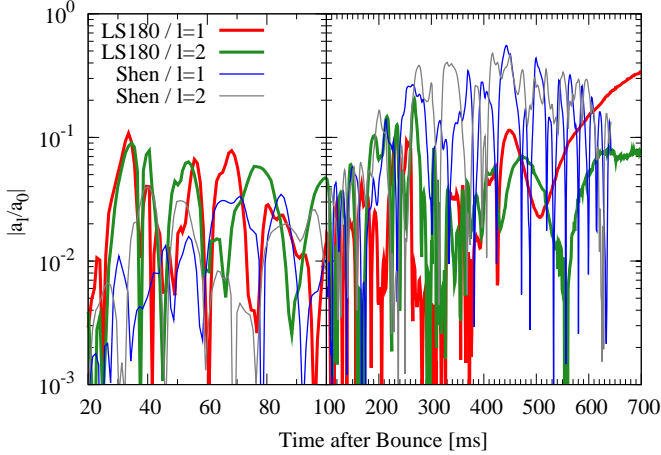


Figure 14. Post-bounce evolution of the amplitude $\ell = 1$ and 2 SASI modes, comparing LS180 (thick lines) and SHEN (thin lines). During the early phase ($t_{\text{pb}} \lesssim 100$ ms) LS180 has a larger amplitude due to the strong prompt-convection activity. Later, LS180 exhibits a smaller amplitude due to the continuously expanding shock wave to larger radii, while SHEN has still an increasing amplitude. However, also for SHEN, it saturates and begins to decrease at $t_{\text{pb}} \gtrsim 400$ ms, indicating a failed explosion.

supernova explosions, e.g., from axial symmetry to three dimensions in parametric studies (Nordhaus et al. 2010; Hanke et al. 2012). The presence of convection and SASI exposes matter in the gain region to net neutrino heating for a longer period. In our models based on LS180, the stronger convective activity leads to more efficient neutrino heating for matter in the gain region such that a higher entropy per baryon is achieved than in the models based on SHEN.

Another important indicator to predict neutrino-driven explosions is the mass enclosed in the gain region (see, e.g., Janka 2001). In Figure 16(c) we find that it is always smaller for SHEN than for LS180 and LS375, because SHEN produces a less compact object

with lower central density and a less steep density gradient at the PNS surface than LS. The mass enclosed inside the gain region reaches its maximum at about 100 ms post bounce, about $0.065 M_{\odot}$ for SHEN and $0.085 M_{\odot}$ for LS. This time corresponds to the time with the maximum accretion rates (see the accretion luminosities in Figure 5). After that, the mass enclosed inside the gain region decreases. After about 150 ms post bounce the enclosed mass in the gain region for SHEN falls significantly below the corresponding values for LS. Note that otherwise the evolutions for SHEN and LS are rather similar up to this moment, see Figure 15, but about 100 ms later they differ substantially. As discussed above, this is a consequence of more efficient neutrino heating for LS due to a higher $\bar{\nu}_e$ luminosity on the one hand and a larger mass enclosed inside the gain region on the other hand. For SHEN, the enclosed mass inside the gain region drops below $0.02 M_{\odot}$ between 200–300 ms after bounce, while it turns around at a value of $0.04 M_{\odot}$ for LS (see Figure 16(c)). As the shock starts to expand for LS only, the gain-region mass differences between SHEN and LS diverge to an extent that it is not meaningful to compare them at a later postbounce time. In summary, the different structures of the protoneutron stars for SHEN and LS lead to a smaller mass enclosed inside the gain region and lower luminosities (mainly $\bar{\nu}_e$) for SHEN. Both effects inhibit the efficiency of the neutrino heating in the models based on SHEN, that do not lead to an explosion in our 2D models.

Additionally the less efficient heating for SHEN can also be related to the absence of large-scale hydrodynamic instabilities. Deformations of the standing-accretion shock assisted by buoyant convections are significantly smaller for SHEN compared to LS180 (compare Figure 9(a) and 9(b)). Moreover, we cannot find any large down-streams of material for SHEN, which for LS180 supply continuously energy to the central regions

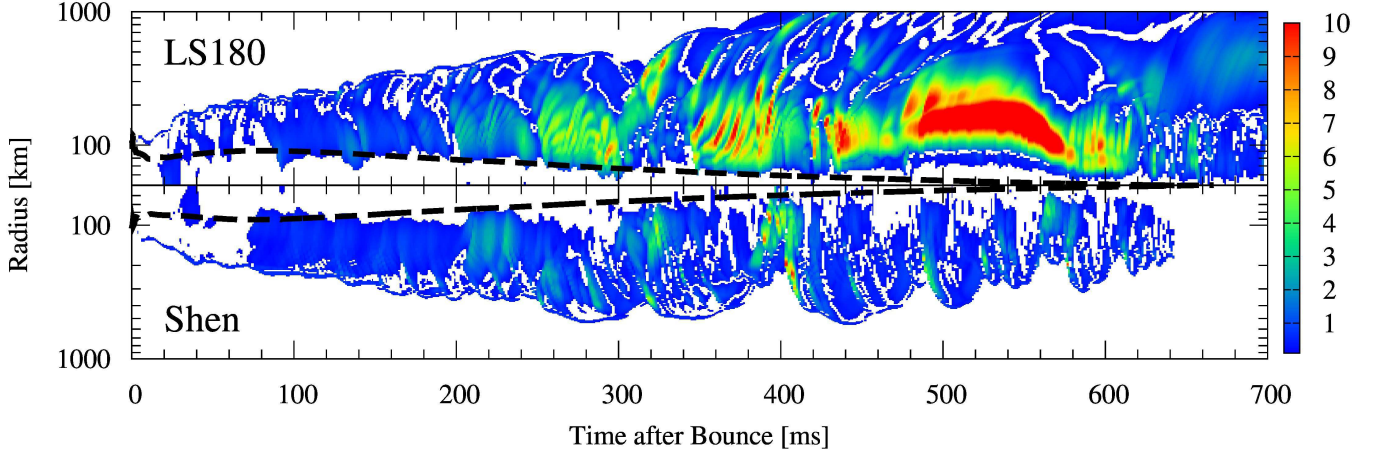


Figure 15. Post bounce evolution of the dispersion of \mathcal{M} (Eq. 15) for LS180 (top panel) and SHEN (bottom panel). The white color is set below the minimum value of 0.1. The thick dashed lines show the position of the neutrinosphere representing the surfaces of the PNS.

in an asymmetric way.

Because the structure of the PNS now appeared several times to stand at the origin between runs using LS180 and SHEN, we wonder whether the radius of the PNS might serve as a reliable explosion indicator. The post-bounce evolution of the PNS radius is shown in Figure 16(d). After the rapid initial rise up to about 90 km for the models using LS180 and LS375, between 10–20 ms post bounce, the PNS radii contract rapidly to about 80 km at about 50 ms post bounce. Using SHEN, the PNS has a smaller maximum radius of 85 km at about 20 ms post bounce. Later, the PNS contracts on a longer timescale on the order of several 100 ms for all EOS, where initially SHEN leads to the smallest PNS radius up to about 200 ms post bounce. After that, the PNS using LS180 contracts fastest and leads to the smallest radius. LS375 has the largest PNS radius during the entire post-bounce evolution. Thus, the PNS radius, which is often used as an indicator of the energy budget available from core collapse, is not a good predictor for the explosion. The same is equally true for the compactness ($GM_{\text{NS}}/c^2 R_{\text{NS}}$).

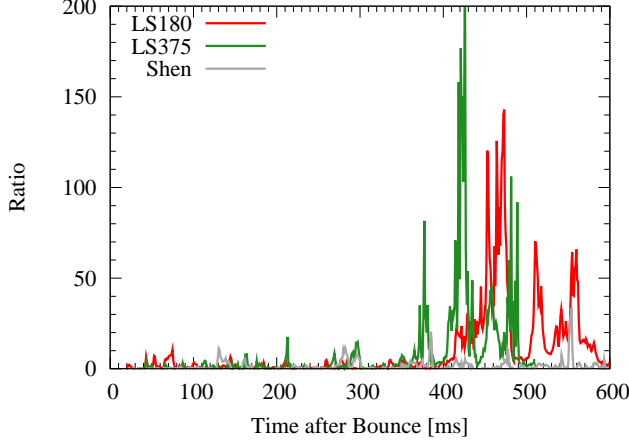
In stead, we conjecture that the time derivative of PNS radius would be more important, i.e., the faster contraction of PNS is better for the shock revival. This is consistent with the discussion of Janka (2012), in which he argued that the smaller PNS radius is better, not faster contraction. It should be noted that in his Figure 4 one finds that the model with smaller PNS radius is identical to the faster contracting model. Therefore, our conjecture (faster contraction is better for explosion) is valid for their simulations.

In Figure 17, we show the ante-sonic condition proposed by Pejcha & Thompson (2012), who suggested that if $\max(c_s^2/v_{\text{esc}}^2) \gtrsim 0.2$,¹² where c_s is the sound speed and v_{esc} is the escape velocity ($=\sqrt{2\Phi}$), the stalled shock will turn to an actively expanding shock front. For the LS EOS we find a rapid increase of $\max(c_s^2/v_{\text{esc}}^2)$ after about 300 ms post bounce, which corresponds well with the onset of rapid shock expansion. For SHEN, $\max(c_s^2/v_{\text{esc}}^2)$ oscillates around its maximum value of about $\lesssim 0.25$ on a longer timescale on the order of several 100 ms.

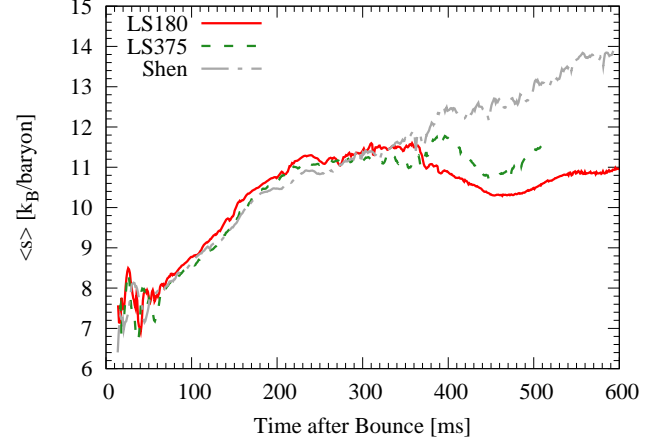
¹² This critical value depends on the microphysics (O. Pejcha, private communication).

Note that the strong spike of this indicator observed for SHEN originates from the multi-dimensional fluid motions (e.g., shock collision with the PNS surface), which is not considered in the 1D analysis by Pejcha & Thompson (2012). The spikes, stemming from a transient local condition, disappear soon by energy redistribution by neutrinos as well as by convective motions. Thus, our result suggests that transient hot spots of the antesononic condition do not suffice to predict an explosion. In order to have predictive power the antesononic condition should be satisfied in a large volume as it is the case in our 2D models based on LS EOS.

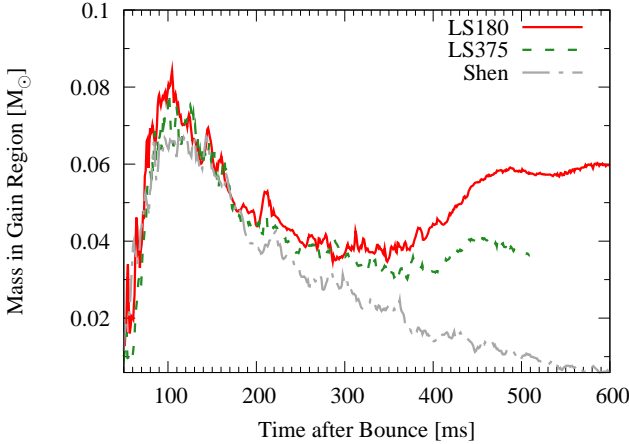
The ratio of the advection timescale (τ_{adv}) and heating timescale (τ_{heat}) is also a well-discussed indicator of the explosion (e.g., Thompson et al. 2005; Buras et al. 2006a; Marek & Janka 2009). This ratio is depicted in Figure 18. If this indicator is greater than unity, i.e., $\tau_{\text{adv}}/\tau_{\text{heat}} \gtrsim 1$, the neutrino heating proceeds fast enough to gravitationally unbind the fluid element, otherwise the matter is swallowed by the cooling region below the gain radius before being heated up. Note that τ_{adv} is determined by the travelling time of mass shells between shock and gain radii. This is an “effective advection timescale”. In 2D simulation, the velocity distribution is stochastic because of the turbulent motion and the SASI activity so that the simple estimate by the velocity profile and radius between shock and gain radii is misleading. Considering a certain mass shell with enclosed mass $M_i(r) \equiv \int \rho dV_r$, where V_r is the volume of a sphere with a radius of r , we note the transit time at the shock and gain radii as $t_{\text{shock}}(M_i) \equiv t(M_i(r_{\text{shock}}))$ and $t_{\text{gain}}(M_i) \equiv t(M_i(r_{\text{gain}}))$, where r_{shock} and r_{gain} mark the shock and gain radii at some time. Then, we determine the advection timescale as $\tau_{\text{adv}}(M_i) \equiv t_{\text{gain}}(M_i) - t_{\text{shock}}(M_i)$. The angular averaged values for the shock and gain radii are used. Moreover, τ_{heat} is estimated by the mass weighted integral of e_{bind}/Q_ν in the gain region, where e_{bind} is the local specific binding energy (the sum of internal, kinetic and gravitational energies) and Q_ν is the specific heating rate by neutrinos. Figure 18 implies that the models with continuous and rapid shock expansion (LS180, LS375) exhibit a more rapid increase of the ratio. For SHEN, the ratio shows also large oscillations with several peaks (even as large as 100). However, this model represents the least optimistic case for possible explosions and hence



(a) Accretion ratio determined by Eq. (18).



(b) Mass-weighted average entropy per baryon in the gain region.



(c) Mass enclosed in the gain region.

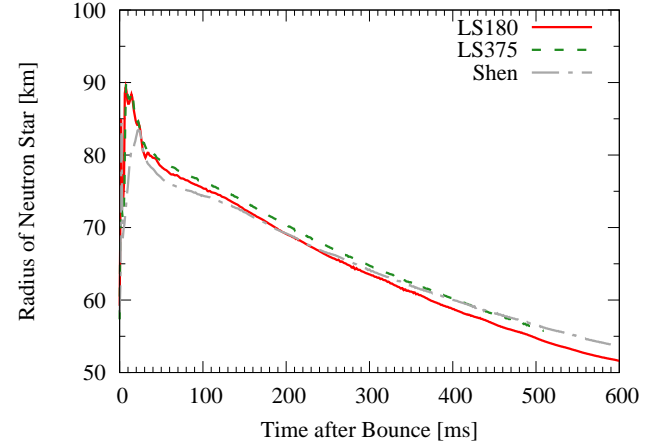
(d) Protoneutron star radii, determined at $\rho = 10^{11} \text{ g cm}^{-3}$.

Figure 16. Post-bounce evolution of selected quantities. In graph (a), the models using the LS EOS have a larger anisotropic downflow, i.e. the ratio becomes larger than 100, while SHEN lies between 0.1 and 10 so that the downflow is rather spherical, slightly oscillating from north pole to south pole and vice versa on a timescale on the order of 100 ms.

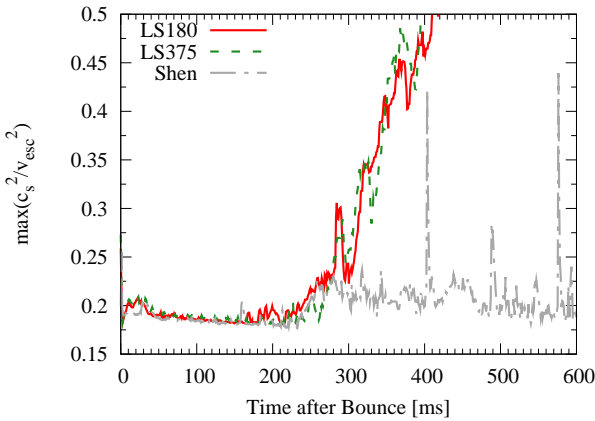


Figure 17. Maximum ratio of the sound speed and the squared escape velocity as a function of time after bounce. The models with a continuously expanding shock (LS180, LS375) satisfy the criterium $\max(c_s^2/v_{\text{esc}}^2) \gtrsim 0.2$, while SHEN shows a very low value with the exception of few transient spikes. The critical value in this case should be raised to $\lesssim 0.25$.

the criteria of the timescale ratio is not a robust indicator for a successful explosion.

Finally, the heating efficiency shown in Figure 19(a)

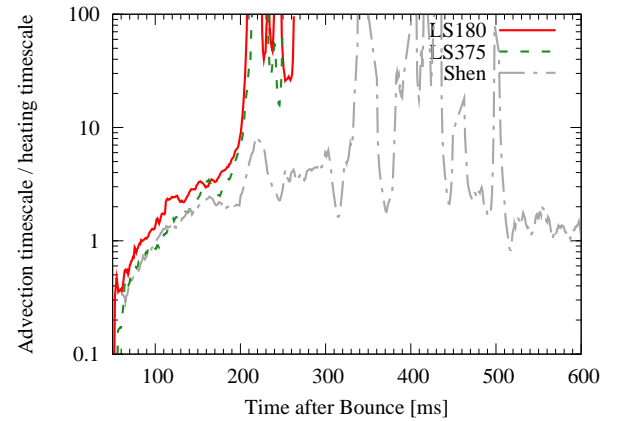


Figure 18. Post-bounce evolution of the ratio of advection and heating timescales. The optimistic models (LS180, LS375) imply a much faster heating than advection through the gain region, while SHEN exhibits several oscillations, which correspond to the shock oscillation and the prolonged dwell time in the gain region.

is used as a measure for the neutrino heating process (Marek & Janka 2009; Müller et al. 2012a). The defini-

tion of the heating efficiency is given by

$$\eta_{\text{heat}} = \frac{Q_{\text{heat}}}{L_{\nu_e} + L_{\bar{\nu}_e}}, \quad (19)$$

where Q_{heat} is the volume-integrated neutrino heating rate in the gain region. We did not find any significant difference for this indicator between models with different EOS. In addition, we show the time evolution of the growth parameter of convection, χ , which is used as an indicator for the onset of the convection induced by the entropy gradient (Foglizzo et al. 2006; Fernández & Thompson 2009; Müller et al. 2012b), defined as

$$\chi = \int_{r_{\text{gain}}}^{r_{\text{shock}}} \frac{\omega_{\text{BV}}}{|v_r|} dr, \quad (20)$$

where ω_{BV} is the Brunt-Väisälä frequency. Foglizzo et al. (2006) showed that χ must exceed ~ 3 for convective motion to grow. Figure 19(b) exhibits the time evolution of χ for investigated models and suggests that EOS does not significantly affect the onset of the convection induced by the neutrino heating.

At this point, we remind the reader again that in this study we omit important cooling and thermalization contributions, i.e. heavy-lepton neutrinos and scattering on electrons/positrons. However, these simplifications affect the evolution of *all* simulations equally. Nevertheless, we find most optimistic conditions for the onset of an explosion in any case, in particular for the $15 M_{\odot}$, using LS180 and LS375. Whether this remains true for LS including these yet missing contributions, will have to be shown in a future exploration. On the other hand, such optimistic conditions were not obtained in ~ 600 ms postbounce for our 2D simulations using SHEN, even without the above mentioned important sources of energy loss. It indicates that it may be much more difficult to obtain neutrino-driven explosions for this progenitor model using SHEN EOS.

4.3. Results of a model with $11.2 M_{\odot}$

In addition to the $15 M_{\odot}$ progenitor from Woosley & Weaver (1995), we performed 2D simulations of an $11.2 M_{\odot}$ progenitor from Woosley et al. (2002). The $11.2 M_{\odot}$ star has been used in several studies before, where neutrino-driven explosions were obtained in 2D (Buras et al. 2006a; Marek & Janka 2009) and 3D (Takiwaki et al. 2012) simulations. Figure 20(a) shows the time evolution of the average shock radius in our 2D models, comparing LS180 (red solid line) and SHEN (grey dot-dashed line). For the $15 M_{\odot}$ progenitor model discussed above, only a passive shock expansion was obtained due to the decreasing ram pressure of LS EOS. In contrast to this, both EOS lead to the successful launch of an explosion in the case of the $11.2 M_{\odot}$ progenitor, for which the expansion of the shock is accompanied by mass outflow. This is illustrated in Figure 20(b), which shows the post-bounce evolution of selected mass shells for the simulation using SHEN. This Figure should be compared with Figure 6, which shows the $15 M_{\odot}$ model using LS180. The differences are caused by the different progenitor structures of the $15 M_{\odot}$ and the $11.2 M_{\odot}$ progenitor models. The latter has a much steeper density gradient

at the interface between the iron core and the Si-layer, as well as between the Si-layer and the C/O-layer. A more detailed analysis regarding the criteria for the successful launch of a neutrino-driven explosion has already been given in Buras et al. (2006a), where the same two progenitor stars have been compared.

For both, SHEN and LS180, the post-bounce accretion phase lasts for only about 50 ms. After this short accretion phase, the shock waves start to expand continuously to larger radii. This is significantly earlier than in the simulations reported by Marek & Janka (2009); Müller et al. (2012a). In the latter, the explosion was delayed by several 100 ms. Our models are not taking general relativistic effects into account and neglect the emission of μ - and τ -neutrinos. Both effects contribute toward a larger radius of the shock in the post-bounce phase compared to models with standard input physics. Moreover, the findings described above in the comparison between SHEN and LS models of the $15 M_{\odot}$ progenitor are seen in the $11.2 M_{\odot}$ model as well. The models based on SHEN lead to less favorable conditions for the explosion. The difference between SHEN and LS180 in the $11.2 M_{\odot}$ model reduces to a slight delay in the onset time of the explosion and a slower shock expansion. As discussed above, it is due to less efficient neutrino heating in the SHEN case. Nevertheless, both explosions are weak. At the end of the simulations, the diagnostic energy is $E_{\text{dia}} \approx 10^{50}$ erg.

A snapshot of the Y_e and entropy per baryon distributions is shown in Figure 21 at 555 ms post bounce. At this this is the last candidate. next esc will revert to uncompleted text. ime the model has already entered the neutrino-driven wind phase, in which regions of constant entropy per baryon emerge around the protoneutron star (see fig. 21). Based on spherically symmetric simulations of massive iron-core collapse and explosions, Fischer et al. (2010, 2011) confirmed recently the expectation of Qian & Woosley (1996), that the neutrino-driven wind attains proton-rich conditions. Our models are consistent with these results: During the early wind phase we obtain $Y_e \sim 0.5 - 0.55$ in the ejected matter.

5. SUMMARY AND DISCUSSION

We performed 1D and 2D radiation hydrodynamic simulations that include spectral neutrino-radiation transfer. The simulations are launched from a $15 M_{\odot}$ progenitor star using four different EOS, corresponding to three different incompressibilities of the LS EOS and one SHEN EOS. LS is based on a non-relativistic approach and has a symmetry energy of 29.3 MeV. The incompressibility parameter can be set to 180 (LS180), 220 (LS220), or 375 MeV (LS375). SHEN is based on relativistic mean field theory and the Thomas-Fermi approximation. It has a symmetry energy of 36.9 MeV and an incompressibility of 281 MeV. This set of EOS represents a wide range of nuclear matter properties.

In 1D, none of the simulations produced an explosion for the considered simulation times up to 1 s post bounce. The observed similarities between LS180, LS220 and LS375, as well as differences to SHEN, concerning the conditions at bounce, the propagation of the shock, and the evolution of neutrino luminosities and mean energies, are in agreement with previous studies. The incompressibility and symmetry energy of the nuclear

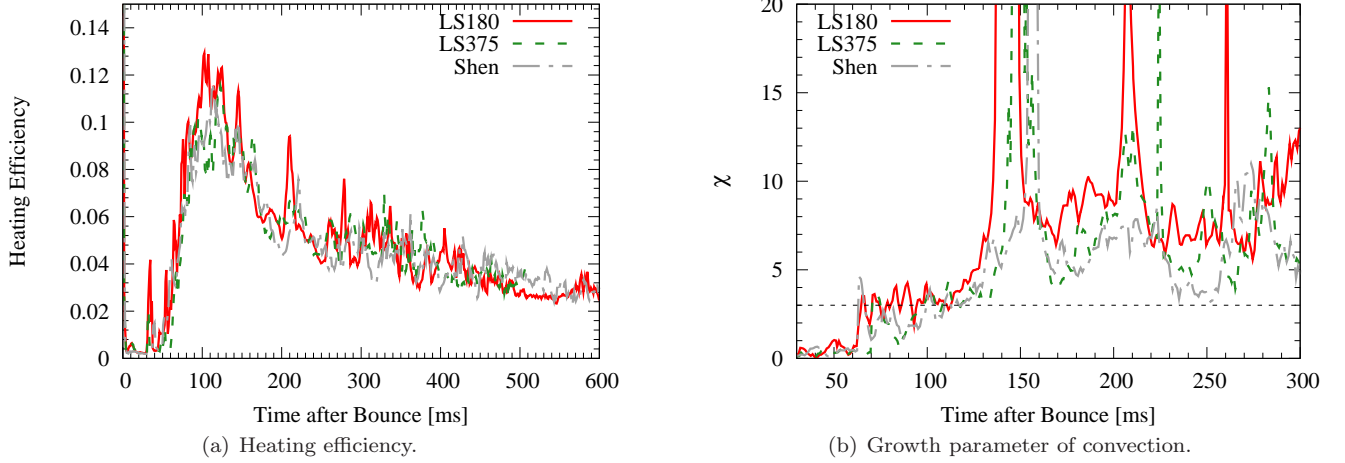


Figure 19. Post-bounce evolution of the heating efficiency (left) and the growth parameter of convection (right). In the right panel, the dotted horizon line represents the critical value of 3. Both quantities do not exhibit the significant EOS dependence.

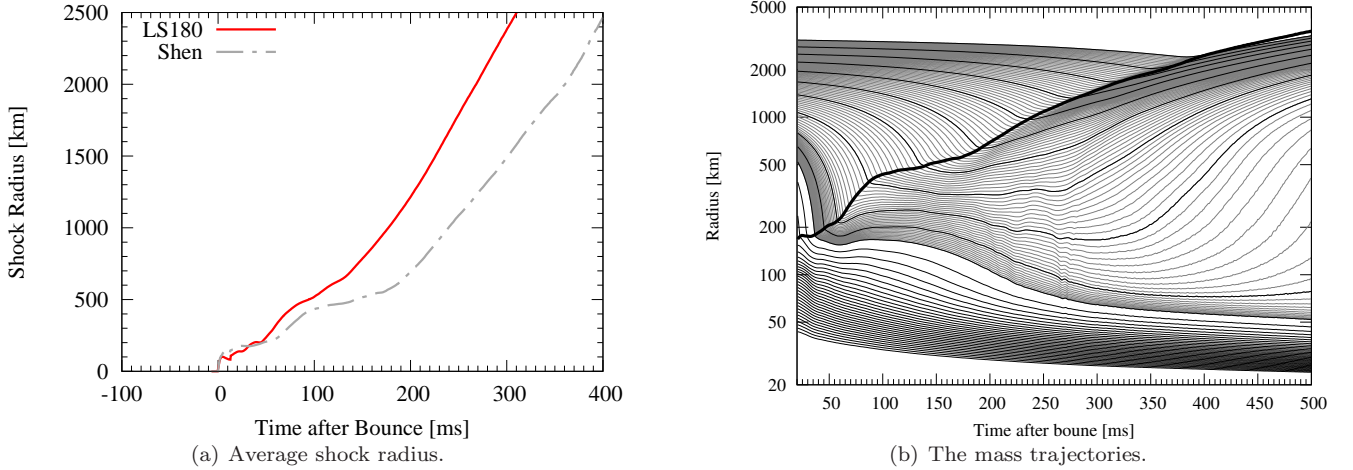


Figure 20. Post-bounce evolution of the average shock radius (left) and selected mass elements (right) for a 2D simulation of a $11.2 M_\odot$ star. In the right panel, the thick black line is the angle-averaged shock radius. The thin black and grey lines show mass elements with an enclosed mass from 1.0 to 1.4 M_\odot (thin black) and from 1.3 to 1.4 M_\odot (grey) at intervals of 0.01 M_\odot (thin black) and 0.001 M_\odot (grey), respectively.

EOS depend on the density and determine the conditions from which the explosion may emerge. However, as recently discussed in Steiner et al. (2012), it is not possible to reduce the characteristics of the EOS to a single important parameter. Note that there are several constraints on the nuclear properties (e.g., Steiner et al. 2010; Lattimer & Lim 2012). These suggest that, among the employed EOS in this study, SHEN has too high symmetry energy, LS180 has too low incompressibility, and LS375 has too high incompressibility. Only LS220 is compatible with terrestrial experiments and the $1.97 M_\odot$ Demorest *et al.* pulsar mass constraint for cold neutron star matter.

In 2D, the differences between models with LS and SHEN EOS are consistent with the differences between the 1D models. For example, we find significantly more favorable conditions for the launch of a neutrino-driven explosion in the models using the LS EOS: The shock expands continuously to large radii, which are not reached in the models using SHEN at comparable times. We an-

alyzed these different post-bounce evolutions and found that models with LS show a highly turbulent velocity field producing prompt convection during the early post-bounce phase. Moreover, LS leads to higher electron antineutrino luminosity and more efficient neutrino heating. More mass is accumulated in the gain region, which leads to a higher entropy per baryon at the early post-bounce phase. In addition, the standing accretion shock instability (SASI) pushes the standing accretion shock to increasingly larger radii after a post-bounce time on the order of 100 ms. In contrast to these models based on LS, the models based on SHEN show weak neutrino heating and the standing accretion shock is only oscillating around a mean radius for simulation times up to 600 ms post bounce. Note, however, that our simulations ignore inelastic scattering on electrons, which is important during the collapse phase, and the emission of heavy-lepton neutrinos, which contributes to the energy loss during the post-bounce phase. These reactions would both make our models more pessimistic, so that

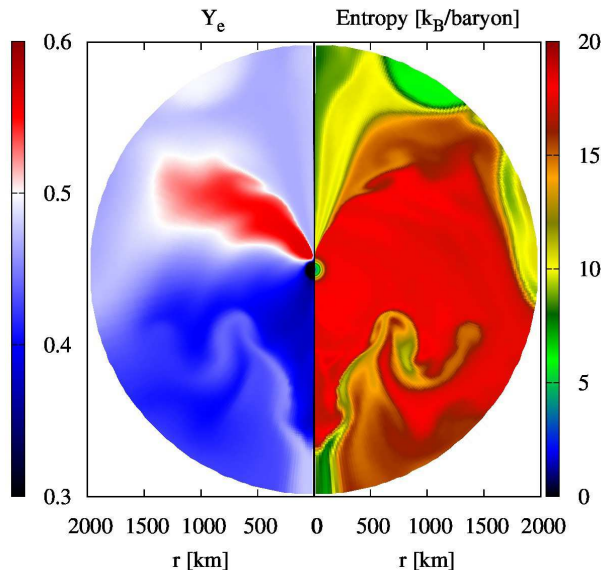


Figure 21. The Y_e (left panel) and entropy per baryon (right panel) distributions of a 2D simulation using SHEN. Shown is a snapshot at the post-bounce time of 555 ms, when the model has already entered the neutrino-driven wind phase.

the 2D models based on SHEN appear unlikely to produce an explosion with the complete set of neutrino reactions. Hence, the different properties of the nuclear EOS can explain some apparently contradictory results found in previous studies, for example the outcome of neutrino-driven explosions in simulations of Buras et al. (2006a); Bruenn et al. (2009); Suwa et al. (2010) using LS EOS and the absence of neutrino-driven explosions in simulations of Burrows et al. (2006) using SHEN. Very recently, Couch (2012) investigated the EOS dependence based on simulations with parameterized neutrino luminosities similar to Murphy & Burrows (2008); Nordhaus et al. (2010); Hanke et al. (2012). He found that a $15 M_\odot$ star is more difficult to explode using SHEN than LS EOS, which is also consistent with the result of this paper.

The most optimistic model, with respect to a possible neutrino-driven explosion, was obtained using LS180, for which we explore different indicators for the possible onset of an explosion. We note again that the neutrino-driven shock revival occurs much faster in this model compared to Marek & Janka (2009) because of the aforementioned neglect of the additional cooling processes. The energy for the shock expansion stems from aspherical mass accretion from large radii deep onto the surface of the protoneutron star, generating a semi-stationary advection cycle. Thus, matter which expands behind the shock wave experiences a continuous flux of neutrinos from the accreted matter. It remains to be shown whether the asymmetry of the accretion pattern is similarly pronounced in three-dimensional supernova simulations. A small difference between the ν_e and $\bar{\nu}_e$ spectra leads to proton-rich conditions. Whether these findings will remain after having included a treatment of charged-current processes that is consistent with the EOS, as discussed recently in Martínez-Pinedo et al. (2012) and Roberts & Reddy (2012), remains to be shown in future studies. Such improvements may become important especially at later post-bounce times that we have not reached in the present simulations.

Based on the described explosion model we evaluate different indicators that have been suggested in the literature to diagnose the onset of an explosion during the post-bounce phase. We confirm that mass-weighted average entropy in the gain region (Murphy & Burrows 2008) and the mass enclosed in the gain region itself (Janka 2001) both show the expected difference between the optimistic LS and the pessimistic SHEN models. With respect to the ante-sonic condition (Pejcha & Thompson 2012), we find that it applies as well. However, fast convection can lead to transient peaks in the indicator that may not be interpreted as a possible onset of the explosion. Also the ratio between advection time scale and heating time scale has been suggested as explosion indicator (Thompson et al. 2005). This indicator is also affected by multidimensional effects and one would have to carefully specify how the time scales have to be averaged in a multidimensional setting. The evaluation of the time scales based on angularly integrated quantities does not lead to a robust indicator for the onset of an explosion. Also the evolution of the radius of the protoneutron star does not serve as a reliable predictor of the explosion.

In order to extend our EOS comparison study to a broader range of initial progenitor models, and in particular to confirm the optimistic results obtained using LS, we also include a lower mass iron-core progenitor of $11.2 M_\odot$ into our investigation. For this model, we obtain neutrino-driven explosions for both LS and SHEN EOS. The differences observed between both simulations remain qualitatively similar to the ones discussed above for the $15 M_\odot$ models. In comparison to LS, SHEN leads to a slightly delayed onset of the explosion with a smaller explosion energy.

However, it should be noted that the simulations in this paper are only a very first step towards more realistic supernova models. In addition to the simplifications of weak processes and the omission of heavy-lepton neutrinos, general relativistic effects should be considered. Additionally, the ray-by-ray approximation may lead to an overestimation of the directional dependence of neutrino anisotropies and of radial oscillations of SASI. A full-angle transport will give us a more refined answer (see Ott et al. 2008; Brandt et al. 2011; Sumiyoshi & Yamada 2012). Moreover, due to the coordinate symmetry axis, the SASI develops preferentially along this axis. It could thus provide more favorable condition for the growth of $\ell = 1$ mode of the SASI and also for the possible onset of explosions along this direction. In the appendix we point to the clear and crucial impact the angular width of the computational domain has on the activity of the SASI, and in consequence on the presence or absence of the explosion. Hence, supernova modelers are gradually switching gears from 2D to 3D simulations (e.g., Iwakami et al. 2008; Scheidegger et al. 2008; Kotake et al. 2009; Scheidegger et al. 2010; Nordhaus et al. 2010; Wongwathanarat et al. 2010; Takiwaki et al. 2012; Hanke et al. 2012; Burrows et al. 2012), in which the SASI and convection were observed to develop much more stochastically in 3D than in 2D. This shows that complementary 3D supernova models are indeed necessary to pin down the impact of the EOS on the neutrino-driven mechanism. Together with the 3D effects, it would also be interesting to study

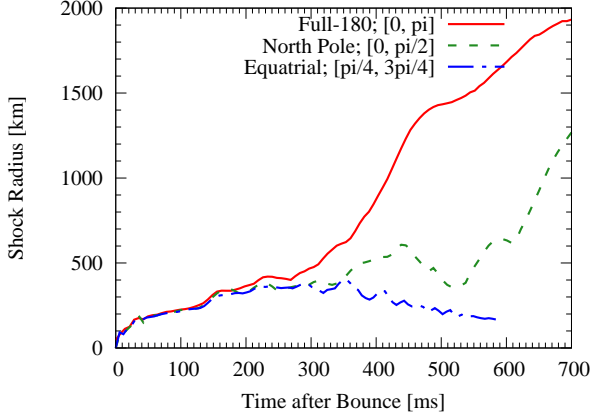


Figure 22. Post-bounce evolution of the average shock radius for different mesh configuration.

the possible EOS impacts on the gravitational-wave signature and neutrino emission (e.g., Marek et al. 2009, Müller et al. 2012, see Kotake et al. 2012 for a recent review). We will address these questions in forthcoming papers.

We thank S. Couch, R. Fernández, M. Hempel, H.-Th. Janka, B. Müller, J. Murphy, T. Muto, Y. Sekiguchi, K. Sumiyoshi, H. Suzuki, and S. Yamada for stimulating discussions. Numerical computations were in part carried on Cray XT4 and medium-scale clusters at CfCA

of the National Astronomical Observatory of Japan, and on SR16000 at YITP in Kyoto University. This study was supported in part by the Grants-in-Aid for the Scientific Research from the Ministry of Education, Science and Culture of Japan (Nos. 19540309, 20740150, 23540323, and 23840023), MEXT HPCI STRATEGIC PROGRAM, the Swiss National Science Foundation under grant (Nos. PP00P2-124879, 200020-132816 and PBBSP2-133378), the HP2C project ‘Supernova’ and HIC for FAIR.

APPENDIX

IMPORTANCE OF SASI

In addition to the full π simulation, we perform simulations with $0^\circ \leq \theta \leq 90^\circ$ and $45^\circ \leq \theta \leq 135^\circ$ for LS180, which shows SASI activity. The latter grid setting was often used in the past, cf., Burrows et al. (1995); Fryer et al. (1999); Buras et al. (2006a). The SASI is thought to be fastest growing for low- ℓ modes, such as $\ell = 1$ and 2 (Blondin et al. 2003). The restriction to $0^\circ \leq \theta \leq 90^\circ$ does not include $\ell = 1$, but it includes the $\ell = 2$ mode, while the restriction to $45^\circ \leq \theta \leq 135^\circ$ does include none of them. Figure 22 shows the post-bounce evolution of the shock average radius for different simulations using LS180 and the three above mentioned resolutions. The red-solid, green-dotted, and blue-dashed lines indicate the full π simulation, $\pi/2$ for the northern pole, and $\pi/2$ around the equatorial plane, respectively. We find that the simulations with $0^\circ \leq \theta \leq 90^\circ$ represent an optimistic case with respect to possible explosions with continuous shock expansion to larger radii. For $45^\circ \leq \theta \leq 135^\circ$, the shock wave does not continue to expand to larger radii and represents the least optimistic scenario with respect to possible explosions. For the latter case, where the development of possible SASI activity is suppressed due to the chosen angular resolution, possible explosions cannot be expected. Thus, large degrees of freedom with respect to angular resolution, allowing for the evolution of SASI, is also an important requirement being able to make predictions about the possible onset of an explosion.

REFERENCES

- Baron, E., Cooperstein, J., & Kahana, S. 1985, *Physical Review Letters*, 55, 126
 Bethe, H. A. 1990, *Reviews of Modern Physics*, 62, 801
 Blondin, J. M., Mezzacappa, A., & DeMarino, C. 2003, *ApJ*, 584, 971
 Brandt, T. D., Burrows, A., Ott, C. D., & Livne, E. 2011, *ApJ*, 728, 8
 Bruenn, S. W. 1985, *ApJS*, 58, 771
 Bruenn, S. W., & Mezzacappa, A. 1994, *ApJ*, 433, L45
 Bruenn, S. W., Mezzacappa, A., Hix, W. R., Blondin, J. M., Marronetti, P., Messer, O. E. B., Dirk, C. J., & Yoshida, S. 2009, in *American Institute of Physics Conference Series*, Vol. 1111, American Institute of Physics Conference Series, ed. G. Giobbi, A. Tornambe, G. Raimondo, M. Limongi, L. A. Antonelli, N. Menci, & E. Brocato, 593–601
 Buras, R., Janka, H., Rampp, M., & Kifonidis, K. 2006a, *A&A*, 457, 281
 Buras, R., Rampp, M., Janka, H.-T., & Kifonidis, K. 2006b, *A&A*, 447, 1049
 Burrows, A., Hayes, J., & Fryxell, B. A. 1995, *ApJ*, 450, 830
 Burrows, A., Livne, E., Dessart, L., Ott, C. D., & Murphy, J. 2006, *ApJ*, 640, 878
 Burrows, A., Dolence, J. C., & Murphy, J. W. 2012, *arXiv:1204.3088*
 Couch, S. M. 2012, *arXiv:1206.4724*
 Dessart, L., Burrows, A., Livne, E., & Ott, C. D. 2006, *ApJ*, 645, 534
 Demorest, P. B., Pennucci, T., Ransom, S. M., Roberts, M. S. E., & Hessels, J. W. T. 2010, *Nature*, 467, 1081

- Fernández, R., & Thompson, C. 2009, *ApJ*, 697, 1827
- Fischer, T., Whitehouse, S. C., Mezzacappa, A., Thielemann, F., & Liebendörfer, M. 2010, *A&A*, 517, A80+
- Fischer, T., Whitehouse, S. C., Mezzacappa, A., Thielemann, F.-K., & Liebendörfer, M. 2009, *A&A*, 499, 1
- Fischer, T., et al. 2011, *ApJS*, 194, 39
- Foglizzo, T., Scheck, L., & Janka, H.-T. 2006, *ApJ*, 652, 1436
- Foglizzo, T., Galletti, P., Scheck, L., & Janka, H. 2007, *ApJ*, 654, 1006
- Fröhlich, C., Martínez-Pinedo, G., Liebendörfer, M., Thielemann, F.-K., Bravo, E., Hix, W. R., Langanke, K., & Zinner, N. T. 2006, *Physical Review Letters*, 96, 142502
- Fryer, C., Benz, W., Herant, M., & Colgate, S. A. 1999, *ApJ*, 516, 892
- Furusawa, S., Yamada, S., Sumiyoshi, K., & Suzuki, H. 2011, *ApJ*, 738, 178
- Hanke, F., Marek, A., Müller, B., & Janka, H.-T. 2012, *ApJ*, 755, 138
- Haxton, W. C. 1988, *Physical Review Letters*, 60, 1999
- Hebeler, K., Lattimer, J. M., Pethick, C. J., & Schwenk, A. 2010, *Physical Review Letters*, 105, 161102
- Hempel, M., Fischer, T., Schaffner-Bielich, J., & Liebendörfer, M. 2012, *ApJ*, 748, 70
- Hempel, M., & Schaffner-Bielich, J. 2010, *Nuclear Physics A*, 837, 210
- Herant, M., Benz, W., & Colgate, S. 1992, *ApJ*, 395, 642
- Herant, M., Benz, W., Hix, W. R., Fryer, C. L., & Colgate, S. A. 1994, *ApJ*, 435, 339
- Hillebrandt, W., Nomoto, K., & Wolff, R. G. 1984, *A&A*, 133, 175
- Hix, W. R., Messer, O. E., Mezzacappa, A., Liebendörfer, M., Sampaio, J., Langanke, K., Dean, D. J., & Martínez-Pinedo, G. 2003, *Physical Review Letters*, 91, 201102
- Iwakami, W., Kotake, K., Ohnishi, N., Yamada, S., & Sawada, K. 2008, *ApJ*, 678, 1207
- Janka, H. 2001, *A&A*, 368, 527
- Janka, H.-T. 2012, *arXiv:1206.2503*
- Janka, H., Langanke, K., Marek, A., Martínez-Pinedo, G., & Müller, B. 2007, *Phys. Rep.*, 442, 38
- Janka, H., & Mueller, E. 1996, *A&A*, 306, 167
- Kotake, K., Sato, K., & Takahashi, K. 2006, *Reports of Progress in Physics*, 69, 971
- Kotake, K., Iwakami, W., Ohnishi, N., & Yamada, S. 2009, *ApJ*, 697, L133
- Kotake, K. 2011, *arXiv:1110.5107*
- Kotake, K., Takiwaki, T., Suwa, Y., et al. 2012, *arXiv:1204.2330*
- Kotake, K., Yamada, S., & Sato, K. 2003, *Phys. Rev. D*, 68, 044023
- Kotake, K., Yamada, S., Sato, K., Sumiyoshi, K., Ono, H., & Suzuki, H. 2004, *Phys. Rev. D*, 69, 124004
- Kiuchi, K., & Kotake, K. 2008, *MNRAS*, 385, 1327
- Langanke, K., et al. 2003, *Physical Review Letters*, 90, 241102
- Langanke, K., Martínez-Pinedo, G., Müller, B., et al. 2008, *Physical Review Letters*, 100, 011101
- Lattimer, J. M., & Lim, Y. 2012, *arXiv:1203.4286*
- Lattimer, J. M., & Swesty, F. D. 1991, *Nuclear Physics A*, 535, 331
- Liebendörfer, M., Messer, O. E. B., Mezzacappa, A., Bruenn, S. W., Cardall, C. Y., & Thielemann, F. 2004, *ApJS*, 150, 263
- Liebendörfer, M., Mezzacappa, A., Thielemann, F.-K., Messer, O. E., Hix, W. R., & Bruenn, S. W. 2001, *Phys. Rev. D*, 63, 103004
- Liebendörfer, M., Rampp, M., Janka, H.-T., & Mezzacappa, A. 2005, *ApJ*, 620, 840
- Liebendörfer, M., Whitehouse, S. C., & Fischer, T. 2009, *ApJ*, 698, 1174
- Marek, A., & Janka, H. 2009, *ApJ*, 694, 664
- Marek, A., Janka, H.-T., & Müller, E. 2009, *A&A*, 496, 475
- Martínez-Pinedo, G., Fischer, T., Lohs, A., & Huther, L. 2012, *arXiv:1205.2793*
- Müller, B., Janka, H., & Dimmelmeier, H. 2010, *ApJS*, 189, 104
- Müller, B., Janka, H.-T., & Marek, A. 2012a, *ApJ*, 756, 84
- Müller, B., Janka, H.-T., & Heger, A. 2012b, *ApJ*, 761, 72
- Müller, E., Janka, H.-T., & Wongwathanarat, A. 2012, *A&A*, 537, A63
- Murphy, J. W., & Burrows, A. 2008, *ApJ*, 688, 1159
- Nordhaus, J., Burrows, A., Almgren, A., & Bell, J. 2010, *ApJ*, 720, 694
- O'Connor, E., & Ott, C. D. 2011, *ApJ*, 730, 70
- Ohnishi, N., Kotake, K., & Yamada, S. 2007, *ApJ*, 667, 375
- Ott, C. D., Burrows, A., Dessart, L., & Livne, E. 2008, *ApJ*, 685, 1069
- Pejcha, O., & Thompson, T. A. 2012, *ApJ*, 746, 106
- Pruet, J., Hoffman, R. D., Woosley, S. E., Janka, H.-T., & Buras, R. 2006, *ApJ*, 644, 1028
- Qian, Y.-Z., & Woosley, S. E. 1996, *ApJ*, 471, 331
- Roberts, L. F., & Reddy, S. 2012, *arXiv:1205.4066*
- Sagert, I., Fischer, T., Hempel, M., Pagliara, G., Schaffner-Bielich, J., Mezzacappa, A., Thielemann, F., & Liebendörfer, M. 2009, *Physical Review Letters*, 102, 081101
- Scheidegger, S., Fischer, T., Whitehouse, S. C., & Liebendörfer, M. 2008, *A&A*, 490, 231
- Scheidegger, S., Käppeli, R., Whitehouse, S. C., Fischer, T., & Liebendörfer, M. 2010, *A&A*, 514, A51+
- Shen, G., Horowitz, C. J., & O'Connor, E. 2011, *Phys. Rev. C*, 83, 065808
- Shen, H., Toki, H., Oyamatsu, K., & Sumiyoshi, K. 1998, *Nucl. Phys.*, A637, 435
- Steiner, A. W., Lattimer, J. M., & Brown, E. F. 2010, *ApJ*, 722, 33
- Steiner, A. W., Hempel, M., & Fischer, T. 2012, *arXiv:1207.2184*
- Stone, J. M., & Norman, M. L. 1992, *ApJS*, 80, 753
- Sumiyoshi, K., & Yamada, S. 2012, *ApJS*, 199, 17
- Sumiyoshi, K., Yamada, S., & Suzuki, H. 2007, *ApJ*, 667, 382
- Sumiyoshi, K., Yamada, S., Suzuki, H., & Chiba, S. 2006, *Physical Review Letters*, 97, 091101
- Sumiyoshi, K., Yamada, S., Suzuki, H., Shen, H., Chiba, S., & Toki, H. 2005, *ApJ*, 629, 922
- Suwa, Y., Kotake, K., Takiwaki, T., Liebendörfer, M., & Sato, K. 2011, *ApJ*, 738, 165
- Suwa, Y., Kotake, K., Takiwaki, T., Whitehouse, S. C., Liebendörfer, M., & Sato, K. 2010, *PASJ*, 62, L49
- Suwa, Y., Takiwaki, T., Kotake, K., & Sato, K. 2007a, *ApJ*, 665, L43
- . 2007b, *PASJ*, 59, 771
- . 2009, *ApJ*, 690, 913
- Takahara, M., & Sato, K. 1982, *Progress of Theoretical Physics*, 68, 795
- Takiwaki, T., Kotake, K., Nagataki, S., & Sato, K. 2004, *ApJ*, 616, 1086
- Takiwaki, T., Kotake, K., & Suwa, Y. 2012, *ApJ*, 749, 98

- Thompson, T. A., Quataert, E., & Burrows, A. 2005, *ApJ*, 620, 861
Thompson, T. A., Burrows, A., & Pinto, P. A. 2003, *ApJ*, 592, 434
Wanajo, S. 2006, *ApJ*, 647, 1323
Wanajo, S., Janka, H.-T., & Müller, B. 2011, *ApJ*, 726, L15
Wongwathanarat, A., Janka, H.-T., & Müller, E. 2010, *ApJ*, 725, L106
Woosley, S. E., Heger, A., & Weaver, T. A. 2002, *Reviews of Modern Physics*, 74, 1015
Woosley, S. E., & Weaver, T. A. 1995, *ApJS*, 101, 181